

Advanced Modeling and Simulation Tools to Address Build-Up Issues in Additive Manufacturing by Cold Spray



Michel Jeandin, Francesco Delloro, and Margaux Bunel

Abstract The objective of the proposed chapter is to discuss recent advances in modeling and simulations for specific application to additive manufacturing by cold spray. To meet the requirements for overall modeling of the process, two scales have to be considered, i.e. that of the powder particle and that of the deposit. These result in two parts in the chapter respectively, i.e. Sections 2 and 3, which follow a rather elaborated introductory section. The latter gives the background and a rapid state-of-the-art in the field of cold spray for additive manufacturing. Experimental and numerical approaches to coating build-up are compared, in particular. The two-fold core of the chapter then highlights both conventional finite element analysis and original morphological modeling of the basic mechanisms involved in cold spray coating build-up. The role of the number of particles to be involved in the simulations is discussed since this number is the key parameter for shape prediction in additive manufacturing.

Keywords Additive manufacturing · Cold spray · Modeling · Simulation · Finite elements analysis · Build-up · Morphological models

1 Introduction

Based on what most of materials science and engineering forums show, all the technological routes seem to lead to additive manufacturing. As all roads lead to Rome, additive manufacturing can, therefore, be said to be Roman and be renamed “Romanufacturing”. Historically, one of these roads/routes comes from the thermal spray, Vardelle et al. [73], e.g. with plasma forming processes. Nowadays, the road from thermal spray to additive manufacturing is all the shorter because the cold spray is

M. Jeandin · F. Delloro (✉) · M. Bunel
MINES ParisTech, PSL Research University, MAT-Centre des Matériaux,
CNRS, UMR 7633, BP 87, 91003 Evry, France
e-mail: francesco.delloro@mines-paristech.fr

M. Jeandin
e-mail: michel.jeandin@mines-paristech.fr

© Springer Nature Switzerland AG 2020
S. Pathak and G. C. Saha (eds.), *Cold Spray in the Realm of Additive Manufacturing*, Materials Forming, Machining and Tribology,
https://doi.org/10.1007/978-3-030-42756-6_5

used, Botef et al. [14]. Cold spray is very attractive because of a high deposition efficiency, which pushes this process at the forefront to compete and/or to complement now-conventional laser-based techniques such as Laser Powder Bed Fusion (LPBF) or Laser Metal Deposition (LMD). The road is also short because a thermal spray operator does additive manufacturing without knowing it. He is like the famous Molière’s character Monsieur Jourdain – nothing to do with Jeandin – speaking prose without knowing it. This results from the mere fact that thermal spray is based on the deposition of material in the form of small-sized elementary components, in other words, powder particles. However, to play in the “big league” among laser-based processes and ride the wave of additive manufacturing, cold spray needs the development of advanced simulation/modeling of deposit build-up for prediction and control of the shape and properties of sprayed parts.

Historically, people have always been fascinated by stacking issues in all fields, i.e. artistic, literary, and scientific with, for example, Arcimboldo, Sade, Utagawa, or Ren Hang (Fig. 1, censored for the latter in this figure). It is therefore quite normal they still fascinate today. The only difference, in the context of additive manufacturing, is that the ingenuity of the previously-mentioned creators is now replaced by numerical simulation: this simulation is coupled with an extensive characterization of the building blocks.

The objective of this chapter, the content of which is given in the abstract, is to show recent advanced development of modeling of the cold-spray build-up process for real additive manufacturing, knowing that cold spray is more and more claimed to be promising in the whirlwind of additive manufacturing [38]. The modeling/simulation route is mandatory for the control of the process to result in the achievement of specific parts, i.e. beyond mere coating application.



Fig. 1 Stacking issues over the centuries, **a** Arcimboldo in the sixteenth, **b** Sade in the eighteenth century, **c** Utagawa in the nineteenth century

2 Background and State-of-the-Art

2.1 Coating Build-up Approach to Thermal Spray

In this section, there is no intention of giving a comprehensive view of modeling of coating build-up in thermal spray. The purpose is more to show a rapid overview of the significant milestones (including the first ones) in the development of deposition models in the field, which will put into perspective those for additive manufacturing by cold spray.

When talking about modeling in thermal spray, a few decades ago, say 25 years ago and over a long time, one thought of work on interaction, between a given sprayed particle and the substrate. Interaction meant impingement and splashing, which involved rapid cooling, solidification and various physicochemical phenomena. Basically, the related studies authored by names synonymous with this type of issues, i.e. E. J. Lavernia, A. Vardelle, M. Pasandideh-Fard, and J. Mostaghimi, resulted in the understanding of splat formation though modeling with some pioneering articles [51, 61, 72]. Anecdotally, a major challenge at this epoch and for a rather long time has been to know the maximum number of splats which could be considered at the same time in a finite element analysis of deposition. At this time, the considered particle was a droplet since spraying was obtained by plasma processing, i.e. prior to the advent of cold spray. From this time, researchers have never ceased to keep forging ahead in this type of approach using more and more powerful computing facilities and related numerical method [13, 50]

In parallel with this finite element analysis of impinging phenomena, other routes were initiated, primarily stochastic modeling [29] which could involve rather conventional Monte-Carlo simulation [46] or original (in the thermal spray field) “lattice-gas” models [20]. The latter was undoubtedly the feeding sap of further development based on mathematical morphology and morphological concepts which were considered to be specifically tailored for cold spray even though works on plasma spraying did not stop (Beauvais et al. [10]). Subsequent works seemed (and continue to seem) to prove the point. When restricting to the morphological approach in line with that elaborated in Sect. 2 of this chapter, the main milestones date back to 2010 and 2014 [23, 37]. The most recent advances in the field, in addition to a comprehensive description of corresponding models, are given in the second section of this chapter, i.e. “Modeling at the scale of the powder particle”. This section shows the so-called “morphological approach”, which combined to a finite element analysis of particle impact, can be claimed to be the decisive step to general modeling of coating build-up by cold spray.

2.2 *Towards Additive Manufacturing by Cold Spray*

Any development in modeling needs validation from experiments. This is the reason why the major requirements for additive manufacturing had (and still have) to be met in parallel. These consist primarily in achieving a high thickness and/or a shape control/mastery for the deposit.

The first requirement for a high thickness, i.e. a high deposition rate, can result in an actual scientific and technological bolt when spraying some specific materials. These are, for example, Al-based alloys for which deposition rate had to be dramatically improved [15]. Fortunately, in the past few years, heat treating the powders was shown to be a suitable solution to remove the bolt [15, 67]. Efforts now focus on industrial feasibility of treating powders, for example using fluidized bed facilities, which, however, is no longer a bolt for the development of cold spray additive manufacturing.

The second requirement, i.e. that for shape control/mastery of the deposit, led to the development of strategies for the nozzle trajectory, possibly including advanced robotics. A significant impetus resulted from works by NRC/Boucherville-Canada up to now [55, 74, 75] as an extension of the tessellation approach to this issue in the pioneering paper by Pattison [62] one decade before. These efforts were pursued by Wu et al. [77] in particular, to name among the most recent examples. These works should be complemented by work on numerical simulation, which can be considered as the 3rd requirement for successful additive manufacturing as a fabrication process as predicted by review and prospective studies of the topic in the key year 2017 [65, 69] in a sort of preview of this same book with this chapter for the modeling part of the build-up issue.

As already said in the introductory part of the chapter, dual modeling of the build-up process, i.e. at the scale of the sprayed particle and at the scale of the sprayed bead respectively, is claimed to be the best for an extended approach to cold spray additive manufacturing. This results in the two subsequent sections in this chapter.

3 **Simulation at the Scale of the Particle**

The process of a cold spray coating formation consists of the iteration of elementary phenomena which are the impact of a particle onto the substrate or onto already-deposited particles. Each impact is characterized by a number of features (e.g. particle shape, size, velocity, temperature, substrate local topography, etc.) which causes a large variability inside the set of possible configurations, even if materials and process parameters are fixed. These elementary events can be considered, as a first approximation, independent. Indeed, it can be shown that, given a typical powder granulometry, feed rates and particle velocities, the probability that two impacts take place at the same time and at the same place is rather low, as shown in [27]. When

looking at the time and spatial scales of these events, experimental observation techniques do not allow nowadays access to any measurement, except in few notable cases that will be introduced later in this chapter. Modeling of particle impact, thus, takes in this perspective all its sense as the only way to access important physical information on what is happening during the process. The scale of particle impacts, both spatial (1 μm and less, depending on the mesh refinement) and temporal (ns), introduces new questions regarding the material behavior: even for well-known metals, as for example Al and Cu, mechanical behavior at the small scale and at extreme strain rates is not known. Moreover, several researchers focused in the last years on the cold spray of non-metallic materials, i.e. ceramics and polymers, thus opening new questions on their impact mechanics and constitutive behavior. A lot of work has still to be done for the understanding of the process when involving those materials, which is likely to involve different elementary phenomena. In this chapter, the focus will be on metals only, since the application of the cold spray technique to this class of materials can be considered more mature, especially from an additive manufacturing point of view. Despite the maturity of some applications, further investigation is still needed to elucidate and model various phenomena at the small scale which are key to the process and not yet completely understood, as dynamic recrystallization, jetting and extreme plastic deformation in localized regions. To this aim, specific physical approaches, involving dislocation dynamics, ultra-dynamic material behavior and polycrystalline plasticity models, need to be studied.

In this chapter section, the focus will be at the scale of the particle. Most of the publications and ongoing works consider particles as made of a homogeneous material, thus neglecting finer scale properties and features, among which the grain structure, dislocation dynamics, twins, shear bands, etc. Three main subjects will be addressed here: powder characterization, impact simulations and morphological modeling (iterative deposit build-up models, i.e. particle by particle).

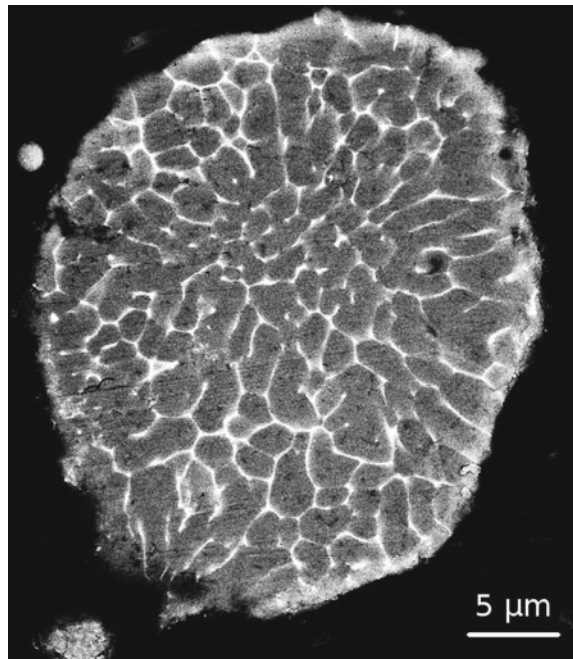
3.1 Powder Characterization

Powders are the feedstock material of the cold spray process and, thus, their properties largely influence the resulting coating. Their production route is fundamental in determining morphological and metallurgical characteristics which, in turn, heavily affect the deposition efficiency and the mechanical properties of the coating. Powders can be characterized in different aspects: metallurgical, mechanical, surface cleanliness and morphological. Nevertheless, most of these characteristics are not independent, because they are all related to the manufacturing process and the thermal history seen by the material. The division made in this chapter, thus, is somehow artificial, but still useful to understand and classify the role that each powder characteristic can assume with respect to the cold spray process.

3.1.1 Metallurgy

The microstructure of powder particles is the result of material composition and of the thermal history, thus reflecting their production route. When dealing with pure metal powders, the main descriptors of the metallurgical state are grain size and shape distributions, dislocation density and internal porosity. In general, particle microstructures can range from dendritic to finely cellular for an atomized powder, as a function of the cooling rate during the manufacturing process. The picture is far more complex for alloy powders, where, in addition to the features already discussed for pure metals, the presence of numerous phases in the form of inclusions and precipitates contribute to the particular microstructure of the material (Fig. 2). An exhaustive discussion of powder metallurgy and its role in the cold spray process is not in the scope of the present work and is already the topic of several research articles. A general review of these issues will be left to future publications. One may say, as a general remark, that alloy powders are extremely sensitive to the production route and to the experienced thermal history, which is the key factor influencing the microstructure. Thus, a great variety of microstructures and, as a consequence, mechanical properties, can be obtained for the same material composition, as a result of manufacturing process parameters and, eventually, post-production thermal treatments [67].

Fig. 2 SEM BSE cross-section image of an Al 2024 particle, produced by nitrogen gas atomization; the grain boundaries are revealed by the higher concentration of alloying elements



3.1.2 Mechanics

Particle mechanical properties come into play at the impact with the substrate or with already deposited particles and are intimately related to the metallurgical state of the material. As a consequence, the interplay between microstructure and mechanical properties is even more complex during the deformation because both characteristics tend to evolve. When colliding, a given particle can undergo extreme plastic deformation, concentrating in the region close to the newly formed interface. In particular, strain and heating rates can respectively reach 10^9 s^{-1} and 10^9 K s^{-1} typically. In these conditions, various microstructure changing mechanisms can occur, i.e. adiabatic shearing instabilities, dynamic recrystallization, melting at interfaces, twinning, dislocation rearrangement and amorphization. For further details, the reader may refer to various comprehensive descriptions, such as those by Moridi et al. [56, 57], Jeandin et al. [40], Cinca et al. [19]. Due to the richness and variety of these elementary phenomena, the modeling of particle mechanics at impact is a very challenging task. The approach generally adopted in the vast majority of the simulations is to neglect the complex microstructure and its evolutions. In this approximation, features at the grain scale or below are not explicitly described and the particle is considered as made of a homogeneous material. In this framework, material behavior can be described by a variety of mechanical models, which will be briefly addressed later on, in Sect. 3.2.1.

Independently of the choice of the material model, a common problem is the origin of the parameter set to be used in cold spray impact simulations. When testing material behavior in the high strain rate regimes, the usual technique is the Split Pressure Hopkinson Bar test (SPHB) (Fig. 3).

One may refer to the voluminous existing literature for an exhaustive description of the technique, for example [28]. Different variations of the test allow for the characterization of the material in compression, tension and torsion. Moreover, the effect of the temperature can also be taken into account in special testing configurations where the sample can be heated. The material model parameters are then identified

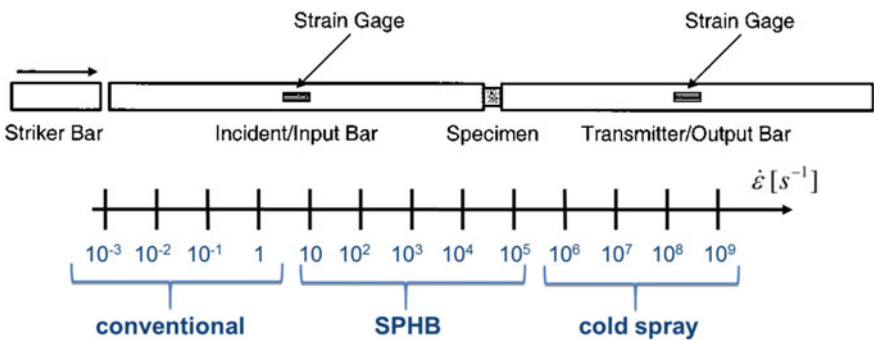
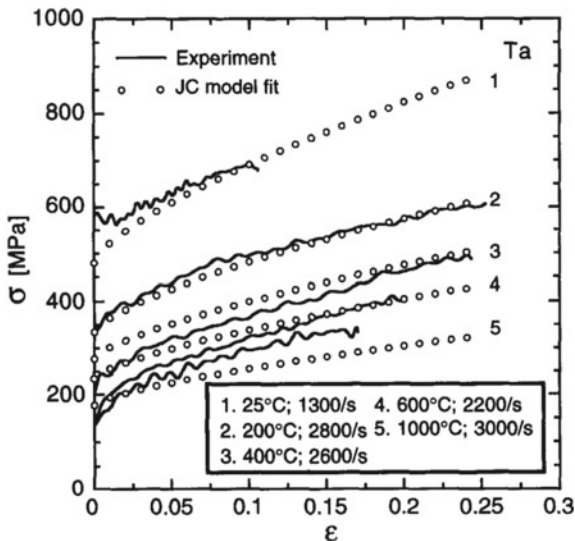


Fig. 3 Schematic illustration of the Split Pressure Hopkinson Bar (SPHB) test, after [28] and comparison of strain rate domains of conventional mechanical tests, SPHB and cold spray

Fig. 4 SPHB test results for Ta at different temperatures and strain rates (curves), while dots represent the numerical simulations with fitted parameters after [18]



by the comparison of simulation results and experimental data obtained through the use of strain gages and post-mortem analysis of the deformed specimen (Fig. 3). In the SPHB test, deformation rates up to 10^5 s^{-1} can be reached. When comparing to typical impact conditions of a particle in cold spray, two critical aspects, namely the size of the sample and the maximum strain rate, can be identified. In one hand, the strain rates experienced by the particles are 3 to 4 orders of magnitude higher (Fig. 4).

On the other hand, the size of the samples is macroscopic for SPHB, consisting usually in cylinders with diameter and height of about 10 mm, while it is 3 orders of magnitude smaller for typical cold spray particles. In addition, the particular metallurgical state of atomized particles, exposed to fast cooling rates, is hardly reproducible in a macroscopic sized sample, as those used in SPHB. The material tested is therefore inherently different, even if the chemical composition might be the same.

From the analysis of what presented here, it is evident that new techniques have to come into play to fill the gap between the macroscopic and relatively slow SPHB tests and particle impacts in cold spray. An interesting alternative is the use of laser shock techniques, which are able to induce mechanical solicitations in regimes comparable to cold spray [9] (Fig. 5a). Recent studies [33] used laser shock to accelerate single particles to velocities in the same range as those attained during cold spray (Fig. 5b) in experiments that can be called LASHPOL (“Laser Shock Powder Launch”). This opens the way to a new experimental framework, where single particle impacts can be produced at controlled velocities. The comparison with numerical simulations of single particle impacts is then expected to result in a reliable set of material behavior parameters, in a procedure known as “reverse modeling”. Having chosen an experimentally accessible goal function (e.g. the particle flattening ratio), the procedure

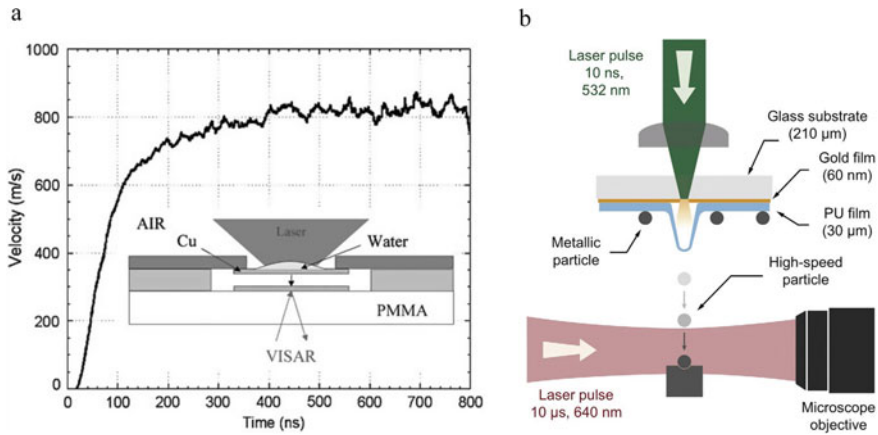


Fig. 5 Laser shock flier experiments and cold spray, **a** high velocity impact of a thin Cu foil onto Al, reproducing the same metallurgical transformations at the interface as observed in cold spray, after [9], **b** high velocity impact of a single particle onto a hard substrate, after [33]

consists in fine tuning the parameters until a good match between experimental and simulation results is obtained (Fig. 6). A recent work moved the first steps in this direction [17].

The identification of material behavior is a complex task and the coupling of different techniques can be beneficial. In particular, a study [7] focused on the quasi-static compression of single particles. A nano-indenter with a flat head was used to this purpose and produced force-displacement data sets which, in conjunction with post-mortem particle shape characterizations and in comparison with the process simulation, allowed to fit the parameters of a strain rate independent constitutive law (Fig. 7). The coupling of static and dynamic techniques will certainly give a richer material characterization than using either one or the other.

3.1.3 Surface Cleanliness

A common problem that every cold spray operator or researcher has surely been confronted to at least one time is to spray an aged powder. Even if properly stored, powders that performed well when fresh tend to lose their ability to adhere to the substrate and to form a coating. This fact suggests that particle surface plays a very important role in cold spray. Different contaminants, inclusions and/or external phases such as oxides, nitrides, etc. can be present at the surface of powder particles (Fig. 8), especially if not properly stored. In particular, external phases are rather easily formed on reactive and oxygen-sensitive materials such as Cu, Ti or Ta [24, 40].

Powder oxidation is a complex phenomenon and its description is behind the aim of this chapter. To remind some of the fundamental processes altering particle surface one may refer to adsorption, dissolution, diffusion and oxide formation.

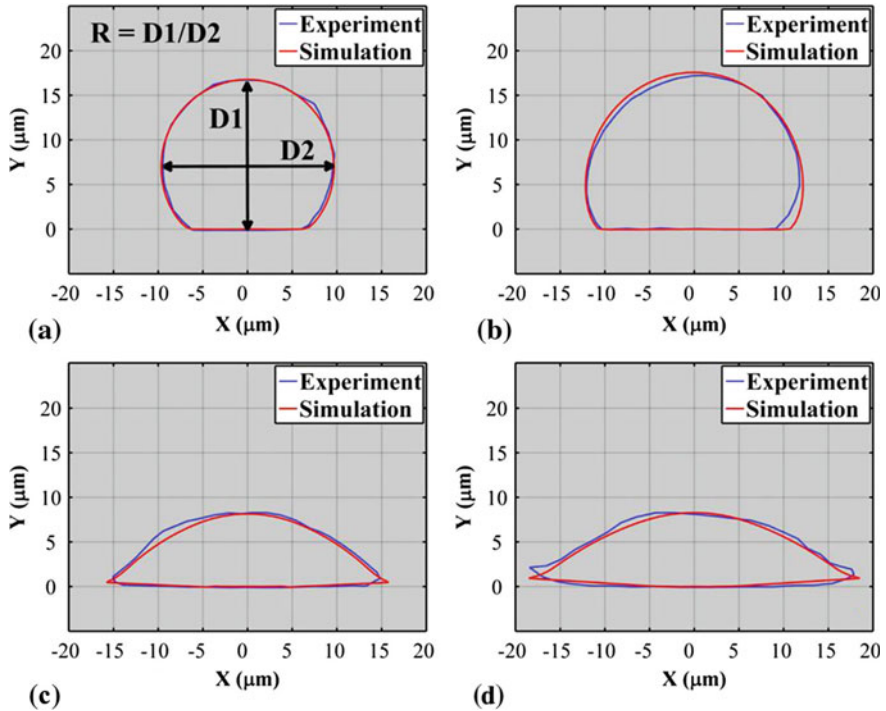


Fig. 6 Comparison of experimentally observed and simulated splat shapes, enabling the tuning of material parameters for a bi-linear Johnson-Cook model, derived from [17]

The kinetic of these phenomena is mainly controlled by their activation energy, temperature and oxygen concentration. Oxidation process starts from the surface but can affect also particle internal microstructure. With aging, the surface oxide layer increases in thickness and oxygen diffusion towards particle interior can take place, thus modifying the mechanical properties of powders via those mechanisms.

In many works on cold spray, adhesion is generally considered as depending on materials and particle velocity: a particle can adhere when its velocity is in an appropriate range, i.e. the so called deposition window [68]. In other words, particle has to flight faster than the critical velocity and slower than the erosion one (Fig. 9). Nevertheless, when looking closer, other characteristics than velocity and material are important with respect to adhesion and surface cleanliness is certainly among these. Naturally, every particle in a powder possesses its oxide layer at the surface, which can be formed during the production process or later, when particles experience contact with oxygen in the atmosphere. Few materials make an exception to this rule, probably gold being one of these.

The oxide layer is hardly avoidable and it is not an insurmountable obstacle. When not too thick, it can be easily broken at impact assuring intimate contact

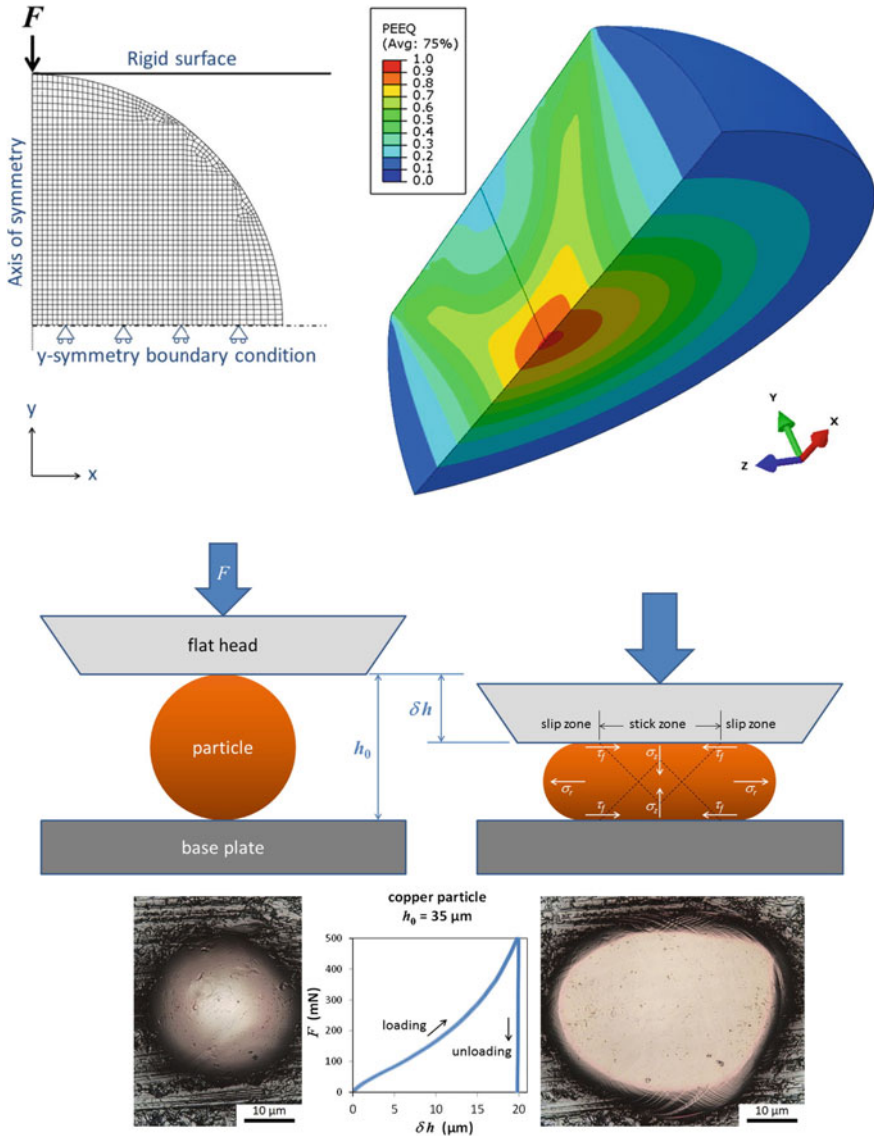


Fig. 7 Schematic illustration of a single particle compression test, after [7]

between the freshly generated metallic surfaces. This is the so-called “oxide break deposition model” which, in combination with the observed material elimination at impact through the jetting phenomenon [27–34], offers a convincing explanation for the experimentally observed metallurgical bonding [35, 48]. Figure 10 shows such a mechanism: during the plastic deformation of the particle and the substrate, the brittle oxide layers locally break, especially in the periphery where the shear strain is

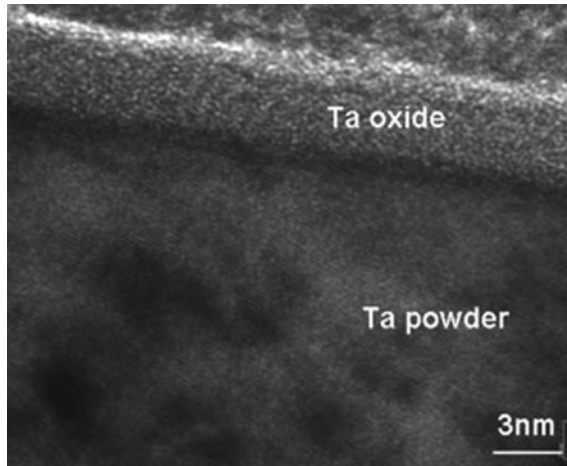


Fig. 8 HR (high resolution) TEM image of a commercial feedstock of Ta powder, after [40]

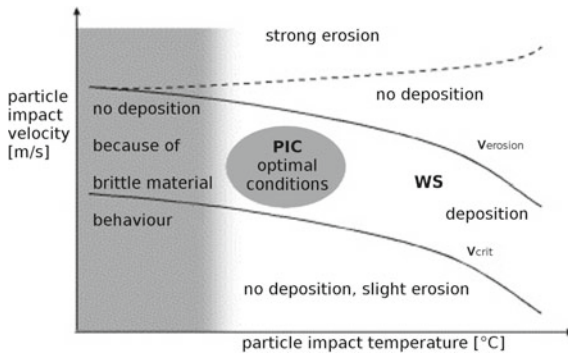


Fig. 9 Window of sprayability as a function of temperature and velocity, after [68]

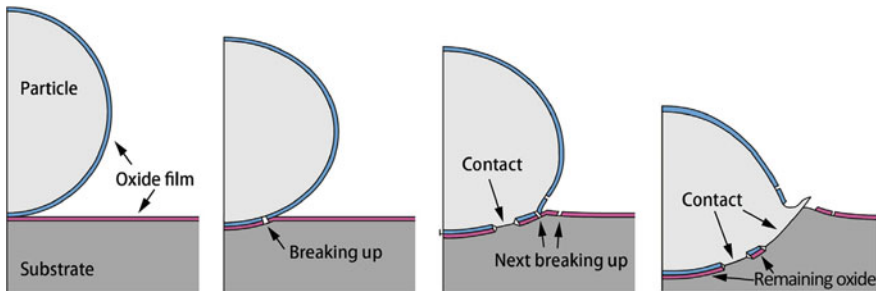


Fig. 10 Schematic view of the “oxide break deposition model”, after [36]

higher. Instead, at the initial point of collision (south pole of the particle), where stress is purely compressive, they were shown [35, 36] to remain intact, thus degrading the local adhesion in that particular zone.

3.1.4 Morphology

The first use of the term “morphology” is attributed to Goethe, in relation to comparative anatomy. We can use it in a similar sense when comparing the external features (i.e. shape and size) of any object and, in particular, of powder particles. When looking at the appearance of different powder samples, one can notice that the morphological features are related to the manufacturing process. For example, water atomization tends to produce irregularly shaped particles and gas atomization more spherical ones, the degree of sphericity being related to the reactivity of the atomizing gas. The most spherical particles are obtained using nitrogen and controlling the surrounding atmosphere, while employing air results in more irregular shapes. Morphological characteristics of atomized powders seem, thus, to be related to the reaction kinetics of superficial oxide formation during the rapid cool down. Other production routes can give more complex morphologies. For example, the most intricate structures are obtained by the agglomeration of smaller particles, which can be made by different materials and contain porosity (Fig. 11a); dendritic or coral shaped particles can be produced by electrolytic methods [5] (Fig. 11b); fused and crashed powders show a very “angular” morphology (Fig. 11c). In these cases, classical observations techniques, as SEM images of the loose powder or cross sections of particles embedded in resin, fail to capture the essential geometrical characteristics, mainly because of their limitation to 2D. In order to give a correct representation of the shape of complex objects, a 3D approach is needed.

In [22], a 3D observation method was developed using X-ray microtomography (XMT) (Fig. 12). XMT is nowadays a well-developed technique, extensively used in many scientific fields and, in particular, in thermal spray as, for example, in [1–3, 31,

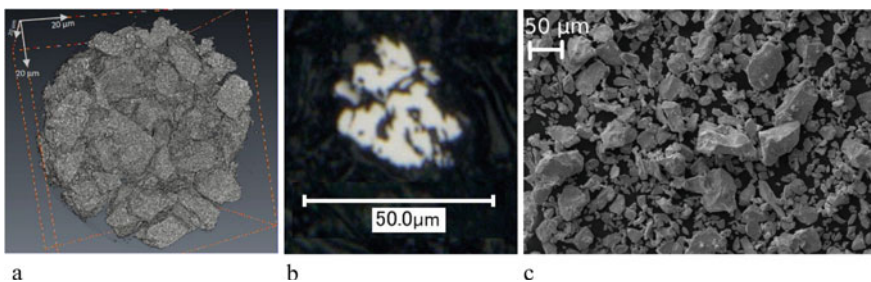


Fig. 11 Exotic particle shapes, **a** XMT image of Ag-SnO₂ powder, Courtesy of Y. Zeralli, MINES ParisTech, 2013, **b** SEM cross section of a coral-like particle, after [52] and **c** SEM top view of the loose tantalum powder Amperit 151.065 (HC Stark, Munich, Germany), produced by the fuse and crash method, after [22]

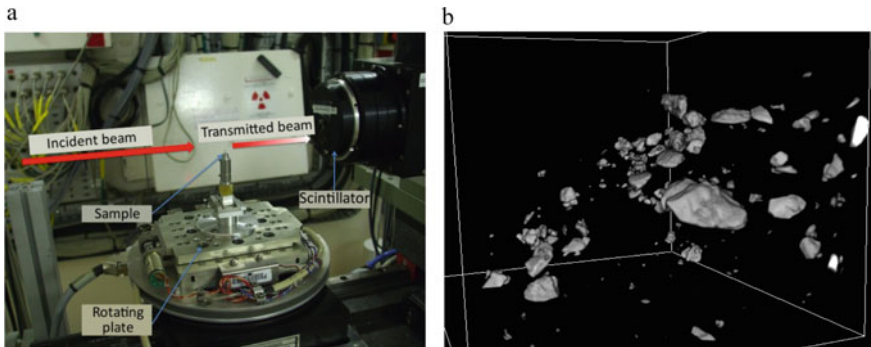


Fig. 12 Application of X-ray micro tomography to powder characterization, **a** experimental set up at ESRF; **b** 3D image after the segmentation showing a volume containing some Ta particles (taken from the powder batch shown in Fig. 11c)

39, 66]. X-rays of a given energy, capable of penetrating the sample through all its thickness, illuminate the material to be observed. The transmitted beam is captured by an imaging device (a scintillator followed by a CCD camera with high resolution, which can be below the μm), resulting in a 2D projection of the volume of the object. The sample is then rotated by a small angle and another image is taken. The iteration of these steps results in a collection of thousands of projections that can be combined in a proper 3D image of the object, through specific algorithms in a process called reconstruction. In the 3D image, the gray level of each voxel (i.e. the 3D analogue of a pixel) is proportional to the local X-ray absorption of the sample. The powder, to assure some distance between particles, was dispersed in a resin and a cylindrical sample suitable for the observation was created. In the reconstructed image of such a sample, metallic particles appeared brighter than the embedding resin. The 3D image needs to be further treated for assigning each voxel either to the powder or to the resin, a process called “segmentation”. At the end of the analysis, a particle library is obtained, made up by all the particles contained in the imaged sample, which could sum up to several thousands.

For certain production routes and, in particular, those giving irregular morphologies, particles can come with a variety of shapes within the same powder batch. A classification method is thus needed for a relevant description of the powder morphology. This was developed, in 3D, in [22], where all particles imaged by XMT were regrouped in a finite set of shape classes (Fig. 13). To achieve this, quantitative shape measurements were introduced, based on the choice of suitable morphological indicators (Table 1), namely MIs. More details on their description and on the classification procedure, which is quite complex, can be found in [22, 31, 60].

To summarize, first an independent set of MIs was created checking the correlations and excluding MIs that were not independent. Then, dimension of the MIs space was reduced applying the Principal Component Analysis (PCA), a technique that consists in linearly combining the MIs and identifying the smallest set of these combinations that assure a good description of the variability of the original data set.

Fig. 13 Particle classification based on morphological criteria, the numbers indicate the number of particles in each class and they sum up to more than 18,000 analyzed objects, after [22]

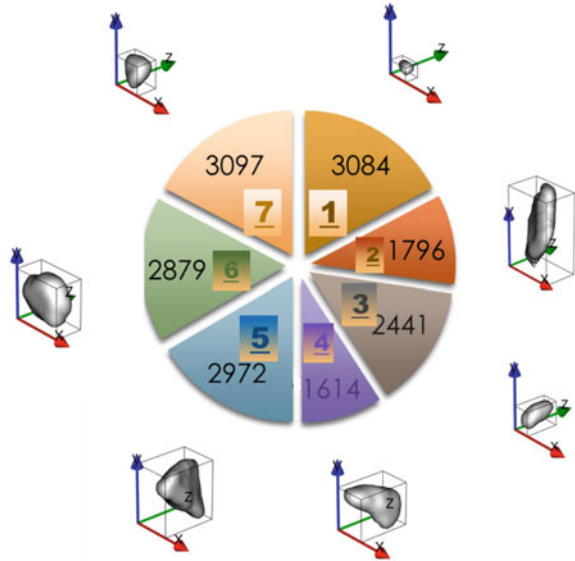


Table 1 Size and shape measures. Underlined parameters are vectors (more than one component) and PAI stands for Principal Axis of Inertia, after [22]

Symbol	Definition
<i>Basic measures (not used directly)</i>	
V	Volume
r_{eq}	Radius of the equivalent sphere: $(3 V/4\pi)^{1/3}$
r_m	Mean radius (mean distance of the surface from the barycenter)
<i>Size</i>	
r_l	$(r_m + r_{eq})/2$
<u>Bb</u>	Bounding box (along PAI) sides
S	Surface
<i>Shape</i>	
r_l	$(r_m - r_{eq})/2$
Sph	Sphericity: volume fraction contained in the equivalent sphere
S/V	Surface over volume ratio
<u>Δ</u>	Normalized PAI: $\lambda_i = PAI_i / (\sum_j PAI_j)$
<u>nbb</u>	Normalized <u>Bb</u> : $nbb_i = Bb_i / (\sum_j Bb_j)$
imbr	Mean imbrication, as defined in [22]

More details are given, for example, in [43]. Finally, the attribution of each object to a predefined shape class was obtained by the K-means cluster analysis technique, an unsupervised classification method, explained for example in [26]. Every particle was assigned to one of the 7 shape classes (Fig. 13). It appeared that certain classes were predominant in volume, meaning that the size distribution was non-homogeneous between classes. It must be noted that particles with a similar shape could actually belong to different classes. In fact, at least in this case, the clustering was a structure imposed on the data and not naturally present from the beginning. The shape varied continuously between particles and the classification was a somehow artificial process, still useful for a clearer understanding of shape data. This implied that two particles belonging to neighboring classes and lying close to the common boundary (on opposite sides) were expected to have very similar shapes and there is no contradiction in this.

3.2 *Modeling of the Impact*

When considering the individual events that, repeated millions of times, constitute the cold spray process (i.e. the impact of a particle), the temporal scale is in the order of 100 ns and the spatial in the range 20–50 μm . If we focus on sub-particle phenomena, investigating for example the deformation localized near the interface, the jetting, oxide layer brake, etc., the scales are even smaller. A part from recent laser based techniques allowing the observation of a deforming particle, as already discussed in Sect. 3.1.2, no direct technique is nowadays capable of giving information on the impact process. For this reason, modeling is the only way to access to the physical quantities of interest, such as temperature, stress, plastic deformation, etc. during the impact. The following part will firstly give a review of some constitutive laws describing the material behavior in the dynamic regime. Then, the most important frameworks for the simulation of impacts will be presented: finite element analysis (FEA) and non-FEA methods. Finally, more specific issues related to impact modeling will be addressed, as the effect of the oxide layer and the influence of substrate surface roughness.

3.2.1 **Material Models**

A number of constitutive laws for material plastic behavior in the high strain rate regime can be found in literature, such as for example Johnson-Cook [8, 25, 41], Preston-Tonks-Wallace [21, 59, 63], Khan-Huang-Liang [17, 44, 45] and Zerilli and Armstrong [6, 79]. The reader may refer to [18, 64] for a comparison of some of them. The interest in such kind of models did not certainly arise with the cold spray technology, because military related studies (ballistic) addressed this field since many decades. The fact that some, if not most, of these results is defense sensitive

can probably explain the difficulty to find extensive and reliable material data for these models.

Due to the extremely dynamical nature of the impact, the use of the Mie-Grüneisen equation of state (EOS) is a common feature. This model, in fact, describes the material state in the high pressure domain and the propagation of shock waves. It can be written as follows, in the so-called Hugoniot formulation:

$$p - p_H = \Gamma \rho (E - E_H) \quad (1)$$

where p is the pressure, ρ the density, E the internal energy, $\Gamma = \Gamma_0 \rho_0 / \rho$, $\eta = 1 - \rho_0 / \rho$, $p_H = \rho_0 c_0^2 \eta / (1 - s\eta)^2$, $E_H = p_H \eta / 2\rho_0$. There are 3 independent parameters for each material in the EOS: η , s and c_0 . Further details on the Mie-Grüneisen EOS can be found in [4].

In the following, we will briefly describe the Johnson-Cook model [41] which is the most widely used for its simplicity. This model is an empirically-based representation of the yield stress and its main advantage is that, due to its popularity, material parameters are available in literature for a large number of materials. The yield stress is given by the following equation:

$$\sigma_{JC} = (A + B\varepsilon^n) \left(1 + C \ln \frac{\dot{\varepsilon}}{\dot{\varepsilon}_0} \right) \left[1 - \left(\frac{T - T_0}{T_m - T_0} \right)^m \right] \quad (2)$$

where A , B , C , n and m are material parameters, ε is the strain, $\dot{\varepsilon}$ is the strain rate, $\dot{\varepsilon}_0$ a reference strain rate, T_m the melting temperature of the material and T_0 a reference temperature. The three factors in the equation take into account respectively the strain hardening, the strain rate hardening and the thermal softening.

3.2.2 FEA Methods

Finite element analysis (FEA) is the most extensively used framework in the simulation of cold spray particle impacts, e.g. among many others [30, 48], and, one could say, in solid mechanics in general. FEA is developed since many decades and comes in a variety of different formulations, each one more or less adapted to address a given problem, ranging from simple elastic and static cases to large deformations, fracture propagation, thermo-mechanical or other multi-physical problems, etc. Many books treating FEA were published and one may refer to them for a thorough explanation of the technique in all its variations. For our purposes, it will be sufficient to mention that FEA is based on the discretization of space in cells, a process called meshing. Inside each cell, the fields (e.g. stress, strain, etc.) are described by some parametric function (typically polynomials), namely the elements.

Two main general formulations can be distinguished, the Lagrangian and the Eulerian. In the first one, the mesh is attached to the material and deforms with it, allowing interfaces to be easily tracked. In the second, the mesh is fixed and the material can flow through it. Eulerian elements may be partially or completely void,

so that interfaces in general do not coincide to element boundaries. For the accuracy of the discretization, it is important for the mesh to be regular, i.e. the cells should have a homogeneous aspect ratio in all directions. In particle impact simulations, the local deformation can be very high, so that the elements in the Lagrangian formulation can be extremely distorted. As a result, the accuracy of the discretization is lost and the simulation could fail due to an excessive distortion of the mesh. A possible solution for this problem is the use of a hybrid formulation, namely ALE (Adaptive Lagrangian Eulerian), which consists in an adaptive meshing tool, performing a regularization of the distorted mesh by displacing its nodes and remapping the fields to the new mesh. This technique proved to be effective in reducing element distortion, but still was not sufficiently robust to easily perform impact simulations (see, for example, Delloro et al. [22]). An important issue linked with the remeshing, was the loss of the correspondence between mesh nodes and material points: the displacement fields were lost in the remeshing steps. This problem could be overcome with the Abaqus® tool called “tracer particles”, which allows following the position of a certain number of material points during the simulation and, thus, retrieving the displacement fields by interpolation.

An alternative technique to ALE is the Combined Eulerian Lagrangian (CEL), also available in Abaqus®. In this framework, the interaction between pure Lagrangian and pure Eulerian domains is implemented. This approach is well suited for complex fluid-structure interaction and large deformations, although it can suffer from the interface tracking issues typical of the Eulerian formulation, especially in multi-particle simulations when the substrate is Lagrangian and the particles Eulerian [76, 78].

3.2.3 Other Non-FEA Methods

Smoothed particle hydrodynamics is a mesh-free discretization technique where the space is divided in non-connected particles, representing interacting mass points. Moreover, they are used for interpolating fields, based on data from neighboring particles, scaled by a weighting function, namely the kernel. Classical conservation equations are then imposed and interaction between particles is set to reproduce plastic material behavior. SPH method, due to its meshless characteristic, is well suited to the large deformations experienced in cold spray (Fig. 14), as shown for example in [49, 53, 54], but suffers from a more expansive computational time compared to Lagrangian FEA.

Another interesting approach, which is relatively new in comparison to all other techniques presented here, is the Discrete Element Method (DEM), which allows modeling simultaneous flow dynamics and growth and microstructure evolution of deposited matter [58]. This framework provides the ability to explicitly track all inter-particle and particle-target collisions and hence provide an alternative to traditionally used methods.

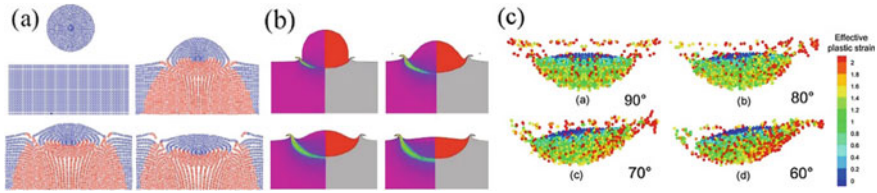


Fig. 14 Impact simulations using SPH. **a, b** Show a comparison between respectively SPH and Eulerian techniques for a Cu particle impacting onto a steel substrate at 700 m s^{-1} , after [53]; **c** SPH method to study the effect of the angle of impact, after [49]

3.2.4 Simulation of Surface Oxide Layers

Few studies dealt with the simulation of oxide layers. In [47] simulations of an Al particle impacting onto an Al substrate in presence of oxide layers, both on the substrate surface and around the particle, were performed using LS-DYNA finite element software, at different velocities (Fig. 15). Three kinds of simulations were performed: without the oxide layer (alumina), with a thin one ($0.4 \mu\text{m}$) and with a thicker one ($0.8 \mu\text{m}$). A brittle behavior was given to alumina by the Johnson–Holmquist plasticity damage model [42]. It was found that the region close to the interface experienced intensive plastic deformation, with its maximum on the sides, far from the initial contact point. The jetting phenomenon could also be simulated, especially for impact velocities higher than 400 m s^{-1} . The alumina layer showed a considerable effect not only at the interface, but in the whole deformability of the particle: oxide break absorbed part of the initial kinetic energy, which therefore was no longer available for the plastic deformation of the metal. A thicker layer thus implies higher particle velocity to have the same material deformation, so that the critical velocity is shifted to higher values.

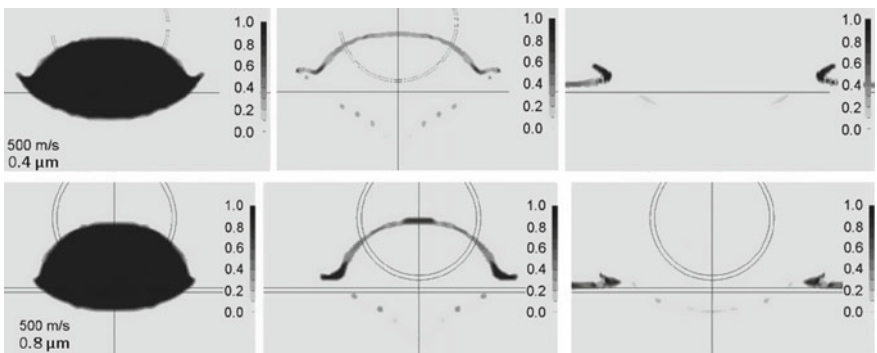


Fig. 15 Simulation results for an Al particle impacting onto an Al substrate at 500 m s^{-1} , with two different oxide layer thickness, respectively 0.4 and $0.8 \mu\text{m}$, after [47]

3.2.5 Effect of Substrate Roughness

Surface roughness is well known to be a key parameter for cold sprayed coating adhesion. Blochet et al. [12] studied the effect of surface preparation by different grades of grit blasting, from an experimental and numerical point of view. In particular, single impact simulations of a pure Al particle onto AA2024-T3 substrate were performed (Fig. 16). A very fine roughness, made up by small peaks and valleys, vanished due to high kinetic impacts. For coarse roughness, the impact onto a valley or a peak gave different results but in both cases the particle could find itself well anchored into the substrate, showing a large contact area. The most prominent surface defects could not be smoothed by particles impact, so that the residual interface roughness was correlated to the initial substrate treatment. The simulations, thus, confirmed the importance of the substrate surface state and helped in explaining the mechanisms favoring particle adhesion.

As a general conclusion, independently of the material couple and of particle velocity, it can be said that the important characteristic determining the outcome of particle-substrate interaction is the relative size of the particle with respect to the characteristic roughness size of the substrate. Three main scenarios can thus be identified (Fig. 17).

1. Macro-roughness (roughness bigger than the particle): equivalent to impact with an angle (the local angle near the contact point).
2. Meso-roughness (roughness at the same scale as the particle): the deformed state can be approximated by the sum of the initial roughness and the deformation induced by the impact on a flat surface (linear combination).

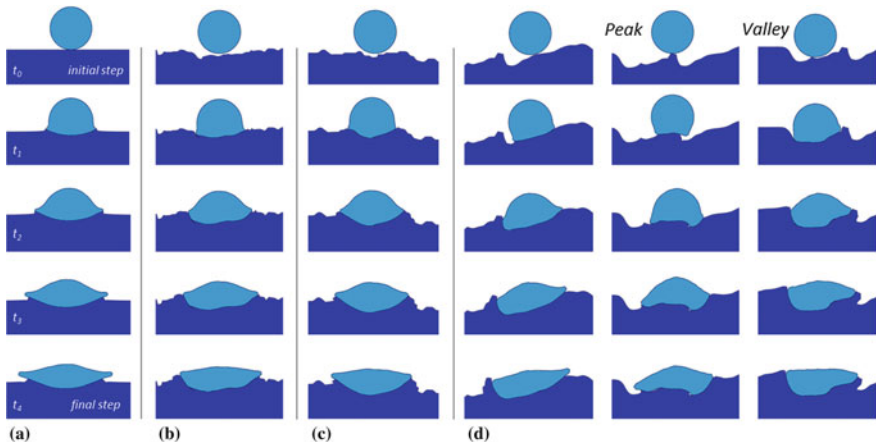


Fig. 16 Effect of the AA2024-T3 substrate roughness at the impact of a pure Al particle (diameter $35\ \mu\text{m}$, velocity), **a** without surface treatment, **b** fine grit-blasted, **c** medium grit blasted and **d** coarse grit-blasted; $t_0 = 0$, $t_1 = 50\ \text{ns}$, $t_2 = 100\ \text{ns}$, $t_3 = 150\ \text{ns}$, $t_4 = 200\ \text{ns}$, after [12]

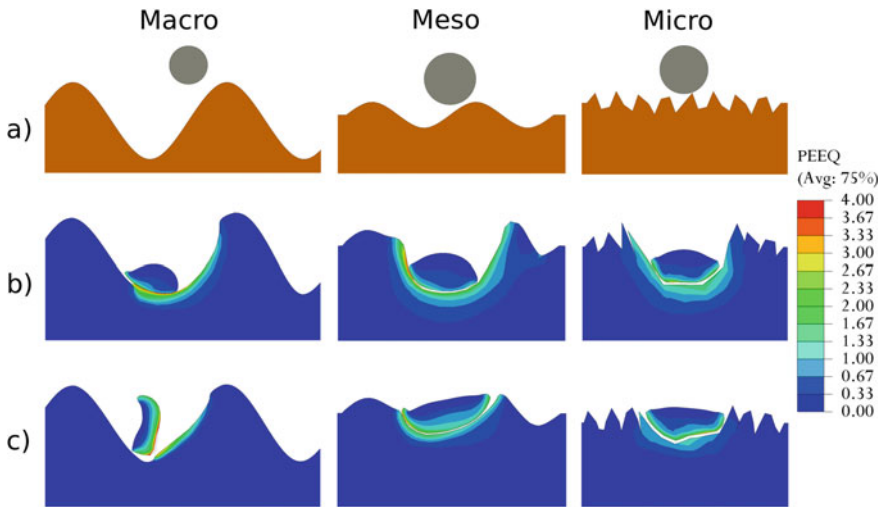


Fig. 17 Effect of substrate roughness at the impact of a Ta particle (diameter $20\ \mu\text{m}$, velocity $500\ \text{m s}^{-1}$). **a** Initial state, **b** after the impact onto a Cu substrate, **c** after the impact onto a Ta substrate; the color scale represents the plastic equivalent strain (PEEQ)

3. Micro-roughness (roughness smaller than the particle): the surface features are simply erased by the impact. As a consequence, deformation is concentrated in the small prominences. When comparing to a flat surface, the small-scale roughness dumps the deformation and penetration of the particle.

3.3 Morphological Modeling

Single particle impact models give rich information on small scale phenomena but, when it comes to the simulation of the build-up of a whole coating, computational costs in terms of CPU time and memory become prohibitive due to the high number of particles involved. Another approach is possible, where coating formation is modeled by adding particles one by one in an iterative mode, miming the building up of the coating. These models are somehow more empirical and phenomenological than single particle impacts because the physical laws are not explicitly considered here. In literature there are very few studies on this kind of modeling, being outnumbered by more classical FEA impact simulations.

In [71] a purely phenomenological 2D model was set up, combining observations of deformed particle shapes and deformation mechanisms. The simulation domain consisted in a regular mesh where particles were added one by one. These were already deformed spheres, thus consisting in ellipses with experimentally measured shape ratios and velocities. When a particle crashed onto the substrate or the forming coating, pixels coming into contact were displaced in a number proportional to the

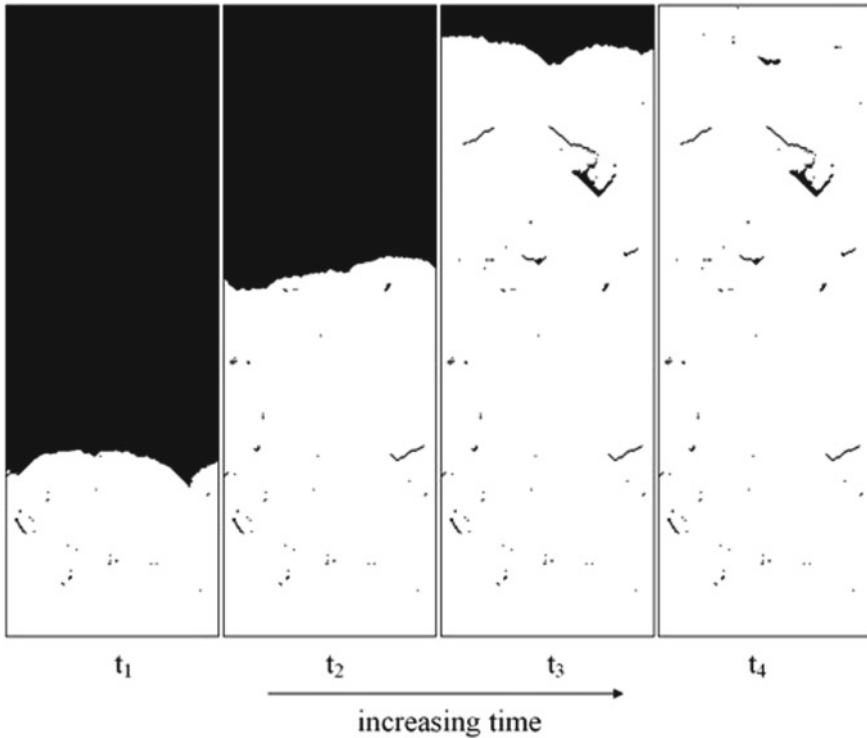


Fig. 18 Iterative coating build up model, for the simulation of porosity in 2D, after [71]

kinetic energy of the particle. After this deformation stage, the particle became part of the coating and a new incoming particle was generated (Fig. 18). This model intended to reproduce porosity formation mechanisms and was tuned to this aim.

A different approach, again miming the coating formation process in 2D by successive depositions of single powder particles, was developed in [22]. Here, data from finite element simulations of single disc-like particle with different sizes impacting with different velocities were combined into a build-up model capable to follow the evolution of the microstructure (splat boundaries). Firstly, a data set consisting of 2D discretized displacement fields was extracted from finite element simulations, constituting the “impact library”. To this aim, the already mentioned tracer particles technique was necessary because remeshing techniques were used. For each simulation, an interpolation of the displacement field was obtained using Delaunay triangulation on the set of displaced tracer particles (Fig. 19) and could be used as a basis for the 2D coating build up model.

To simplify (more details can be found in the original paper), the coating build-up model consists in the iteration of the following steps. First, a particle impact is chosen from the “impact library”, thus selecting a particular displacement field. Then, the substrate, with the already deposited particles, is deformed as dictated

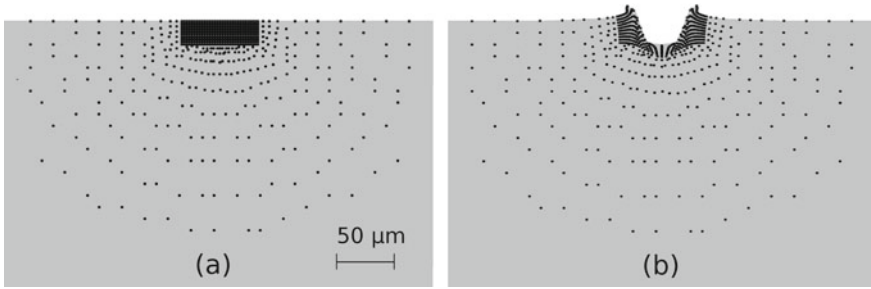


Fig. 19 Positions of tracer particles, before (a) and after (b) particle impact, after [22]. Only the substrate is shown here, in gray

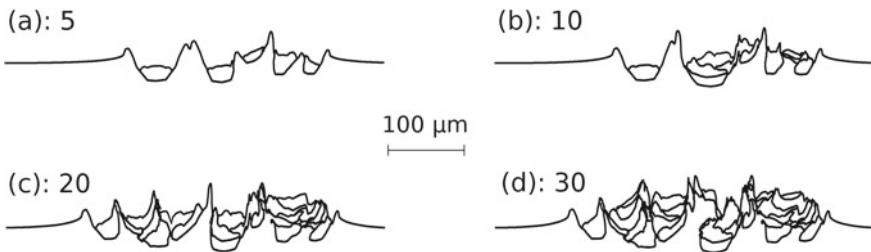


Fig. 20 Results of the coating build up simulation, after 5 (a), 10 (b), 20 (c) and 30 (d) iterations, after [22]

by the interpolated deformation field. Finally, the impinging particle is added. This procedure can then be repeated, in an iterative way, up to a large number of particles (Fig. 20). This modeling approach showed to be powerful and promising for the simulation of the cold spray process. Nevertheless, many features have yet to be introduced in the model, as for example a full 3D approach and the effects of the substrate roughness.

4 Modeling at the Scale of the Deposit

A major drawback in the finite element (FE) analysis of the coating build-up rests on calculation times. For this reason, to scale up from the particle dimension to that of the deposit needs to move on to simulation methods other than those based on finite elements. Section 2 in this chapter showed the use of advanced statistical methods to complement previous a FE analysis. This ideal dual two-scale approach to build-up still remains to be completed despite recent significant progress. Besides this dual approach, recent FE-free direct simulation at the deposit scale was developed, as considered in this third part of the chapter. The first target to be met in this development was computing time reduction. Better flexibility and efficiency are

expected from this reduction to result in a tool to be used in the additive manufacturing context, even though this could be to the expense of accuracy. This means that the subsequently-described simulation relates to a global description of the deposit geometry rather than that of what occurs at the scale of the particle. Unlike in the morphological modeling which was shown in Sect. 3.3, there is no input from particle characteristics which would require too high computing capabilities.

4.1 Fundamentals and Assumptions for Simulation of Deposition Build-Up

4.1.1 General

The core principles of this build-up model are to claim that the spray angle does govern the build-up process. This is quite in keeping with the additive manufacturing process in which the role of the shape of the deposit is prominent for both the (build-up) process itself and its result. The term “spray angle” is to be understood in its broadest and most diverse sense. This includes that of conventional spray angle and that of impact angle, which relate to the nozzle and to the elementary particles respectively. As could be guessed, the deposition efficiency is behind this notion of angle through the implicit involvement of the particle rebound phenomenon.

In practice, the simulation from the model consists in building-up of successive beads (i.e. one-pass deposits), the profile of which was determined initially. The model/simulation was developed in a 2D first then extended in a 3D (or more exactly, a pseudo-3D) version. A great part of the discussion in this section will be based on 2D results to alleviate the approach. The 3-dimensional part will be considered mainly at the validation stage. Moreover, the model was tested using Al 2024 (Aluminum 2024 Alloy) powders. These powders had been heat treated prior to spraying to result in a high deposition efficiency to be suitable for additive manufacturing as discussed in Sect. 2.2. All conditions for heat treatment and for subsequent cold spray are given in (Bunel et al. 2016). Unless otherwise specified, anything which follows will refer to these experimental conditions. To give an idea of the experimental cold spray parameters which were used, one may however mention the main cold spray parameters, i.e. a powder low rate of 15 g min^{-1} , a stand-off distance of 30 mm, a pressure of 5 MPa, and a temperature of $450 \text{ }^\circ\text{C}$.

These considerations led to the establishing of the two basic elements of the model, i.e. the deposition efficiency versus spray angle curve and the one-pass deposit (cross-sectional) profile. It is thus understood easily that the model therefore involves a scale higher than that involved in conventional FE analysis (Sect. 2), i.e. thousands of particles rather than given elementary particles.

The overall simulation route therefore results in 3 steps (Fig. 21).

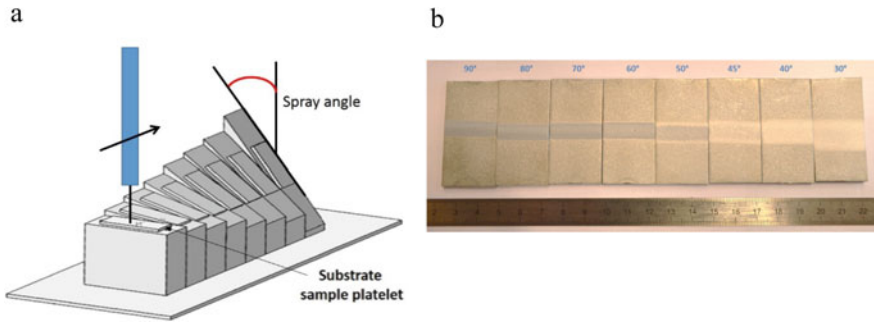


Fig. 21 Cold spray at various spray angles, **a** schematic illustration of the specific experimental set-up, **b** optical top view of the central sprayed beads onto the platelets (of 2.5 mm thick) as a function of spray angle

The first step is a spraying stage made of spraying tests to achieve beads (made of single pass deposition) for given spray angles. Incidentally, with a spray angle as defined in Fig. 21, perpendicular spraying corresponds to a spray angle of 90°.

The second step is the characterization of as-sprayed beads, which leads to the two master curves of the model, i.e. the so-called “nominal” bead profile (Fig. 22a), i.e. for a normal incidence of the nozzle, and the deposition efficiency versus spray angle curve (Fig. 22b).

The third step is that for application of the developed computing code, which results in a typical calculated profile for a deposit which can be achieved onto a large area from multi-passing of the nozzle (Fig. 23). In Fig. 23, this profile is given for perpendicular spraying (i.e. for a spray angle of 90°). The corresponding spraying parameters (those relevant to the code) are given when required.

The parameters relevant to the model and simulation are the kinetic parameters linked to the displacement of the cold spray nozzle, i.e.:

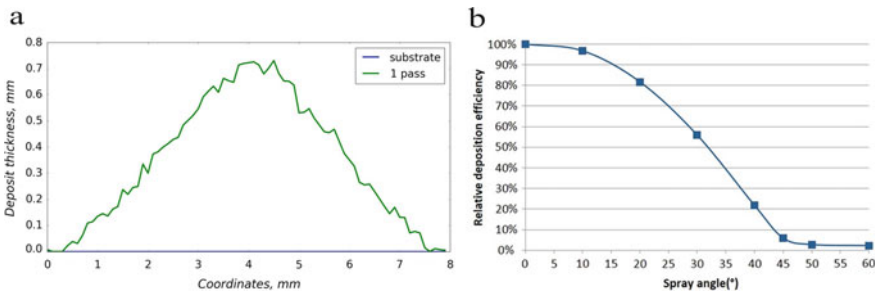


Fig. 22 Input curves for simulation, **a** nominal bead profile, i.e. deposit thickness versus (x, y) coordinates, **b** deposition efficiency (D.E.) versus spray angle

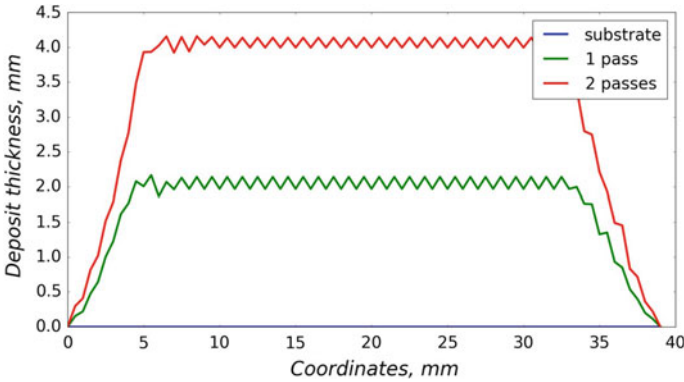


Fig. 23 Example of simulated profiles, for 1 and 2 passes

- The *traverse speed*, i.e. nozzle passing velocity (relative to the substrate).
- The *number of passes*, knowing that a pass is defined as the whole trajectory of the nozzle which leads to an elementary layer, e.g. the whole slotted track in a given color (read or blue) in Fig. 24. The blue and red tracks in Fig. 24 were consecutive and therefore corresponded to even and odd passes respectively, for example. The starting point of a given pass is the same as that of the previous pass in the same series, i.e. odd or even.
- The *step size*, i.e. the width (arrowed in green in Fig. 24) of an elementary up and down in the slotted nozzle track.
- The *spatial shift*, between 2 successive passes, taken as half of the step size, for example, in the subsequent discussion of the model.
- *Possible direction reversal* for nozzle passing after every pass. If not, at the end of a given pass, the robot track moves outside of the area to be coated and goes back to the starting zone of the substrate for subsequent passing.

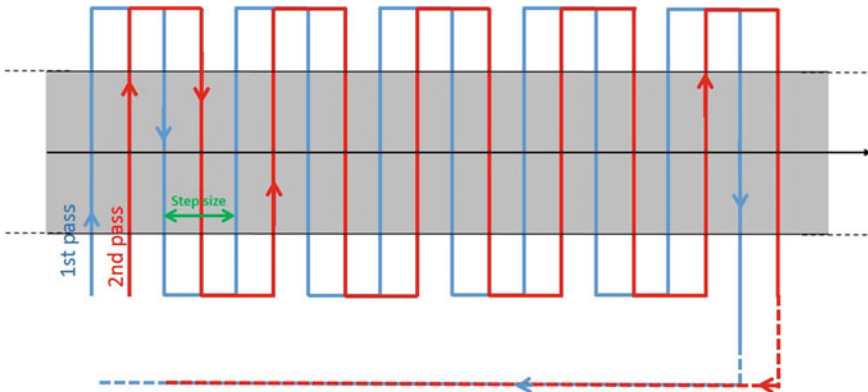


Fig. 24 Schematic top view of nozzle passing showing the key parameters for simulation

The result of the two-dimensional simulation must be compared to observation from a transverse cross-section along the longitudinal axis (black line) of the area (in gray) to be coated (Fig. 24). Every 2D profile after a given pass can be achieved and visualized (e.g. for 2 passes in Fig. 23). The model leads to simulation of the coating thickness and roughness and their evolution as a function of the number of passes. It starts from real build-up profiles and can use robot trajectory parameters to result in the prediction of the final shape of the deposit. The simulation process is therefore opposite to what can be encountered in robot programming. When programming a robot, one starts from the targeted geometry of the part and the smoothed bead profile to infer the robot trajectory [16].

The subsequent sub-sections show how the two key parameters of the model, i.e. bead profile and impact angle, are involved to result in simulation inputs. Their processing conditions and influence will be discussed.

4.1.2 Bead Profile

The nominal bead profile consists of a building block, the characteristics of which, primarily the height and the width, depend on the cold spray processing conditions and therefore integrate them. A given profile therefore corresponds to a given set to spraying parameters. Among these parameters, the stand-off distance has only little influence provided that its variation remains rather limited.

A given profile is discretized prior to be used as an input to the model. The profile is thus made of a series of n height bars at given coordinates (bright vertical lines in Fig. 25). The height of the n th bar is h_n and the distance between 2 successive bars is the discretization interval. The calculation step, consequently the computing time and precision of the model, depends on the discretization interval.

By definition, the value of the calculation step cannot be lower than that of the discretization interval. In contrast, the reverse is acceptable. For example, for a discretization interval of $20\ \mu\text{m}$, the calculation step will be taken as a multiple of $20\ \mu\text{m}$, e.g. $20, 40, 60, \dots\ \mu\text{m}$. The calculation step must not be too low for two reasons. The

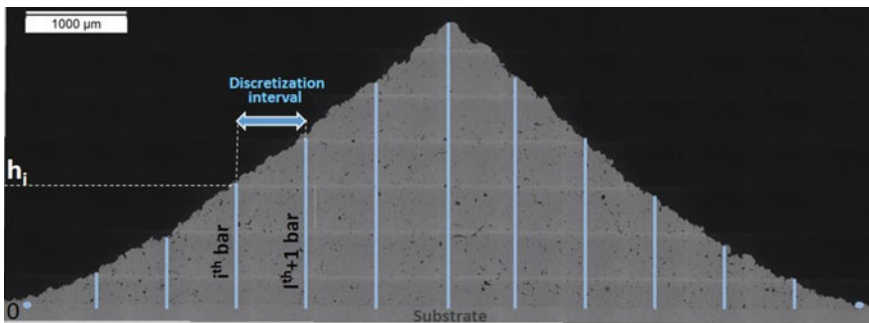


Fig. 25 Discretization of a given experimental deposit profile (2D cross-section)

first reason results from the fact that the lower the calculation step, the more precise the model is but to the expense of the computing time, the latter being proportional to the calculation step. The second reason relates to the powder particle size, which governs the roughness of the bead profile, due to a random particle build-up process. Choosing a calculation step rather higher than the mean particle size can limit the influence of this same roughness. For example, when using a powder with a $D_v(50)$ of 20 μm , it is recommended not to use a calculation step lower than 100 μm .

4.1.3 Impact Angle

Unlike the conventional spray angle as previously defined in Fig. 21, the impact angle is a local parameter. It corresponds to the actual angle with which the sprayed particle collides the substrate. This angle therefore depends on the profile outline at a given build-up time and refers to the local slope at the point of impact in the profile outline. At the first pass for the achievement of the first bead, i.e. starting from a flat substrate, the impact angle is the same as the spraying angle. However, as from the first overlap when moving back the nozzle after the first bead, the impact angle evolves due to changes in the substrate geometry.

The spray angle has a great influence on deposition efficiency (Fig. 22b) through the variation of the degree of rebounding [11]. Deposition efficiency is all the lower as the spray angle decreases. The impact angle shows the same trend. Consequently, the impact angle has to be calculated prior to every nozzle pass to result in the proper height increment for deposit. The calculation of the impact angle at the n th discretization coordinate involves that of the difference between the height of the deposit at this same coordinate, i.e. h_n , and, on one hand, the height of the previous coordinate, i.e. h_{n-1} , and, on the other hand, the height of the subsequent coordinate, i.e. h_{n+1} . The signs of the two resulting height differences, namely d_{n-1} and d_{n+1} , depend on that of the corresponding slopes.

$$d_{n-1} = h_{n-1} - h_n \quad (3)$$

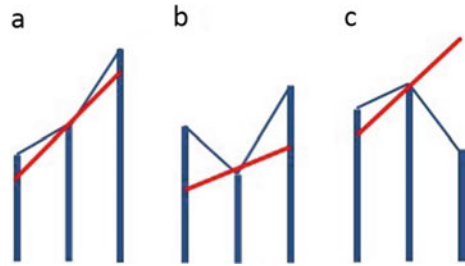
$$d_{n+1} = h_n - h_{n+1} \quad (4)$$

Three cases are to be envisaged according to the respective signs of the height differences, which correspond to (Fig. 26):

- A mere slope when d_{n-1} and d_{n+1} are of the same sign
- A valley when d_{n-1} is positive whereas d_{n+1} is negative
- A peak when d_{n-1} is negative whereas d_{n+1} is positive.

The overall difference must involve offsetting, i.e. positive offsets for valleys and negative offsets for peaks, but nothing for conventional slopes. The implementation of this offsetting system resulted from considering that material deposition was easier in a valley in which the angle decreased gradually rather than on a peak.

Fig. 26 Schematic illustration of the calculation process for the impact angle in the 3 possible geometries



Consequently,

- For slopes and valleys, the overall difference takes the following value of:

$$d = |d_{n-1} + d_{n+1}|$$

- For peaks it takes:

$$d = |d_{n-1} - d_{n+1}|$$

The impact angle can thus be calculated using the mere following expression:

$$\alpha = 90 - \arctan\left(\frac{d}{x_{n+1} - x_{n-1}}\right) \tag{5}$$

where x_n is the coordinate of the n th bar along the x-axis in the 2D bead transverse cross-section (Fig. 25).

Once the impact angle is calculated at a given point, the height of the deposit to be added takes into account the deposition efficiency curve (Fig. 22b) using the rule of proportionality. For near-normal angles, the height to be added will remain nearly the same as previously. In contrast, for rather low angles, the height can decrease significantly. The effect of the involvement of the impact angle in the model is significant, as shown on the example of deposition using conventional cold spray conditions for Al 2024 with a step size of 1 mm (Fig. 27), starting from a typical bead profile such as that in Fig. 25.

The involvement of the impact angle as determined using the previously-described rules is therefore crucial at every calculation step in the model.

4.2 Influence of Basic Model Parameters

The basic parameters of the models were defined in Sect. 3.1.1. To be relevant, all discussions for comparison between the influences of the parameters of the model

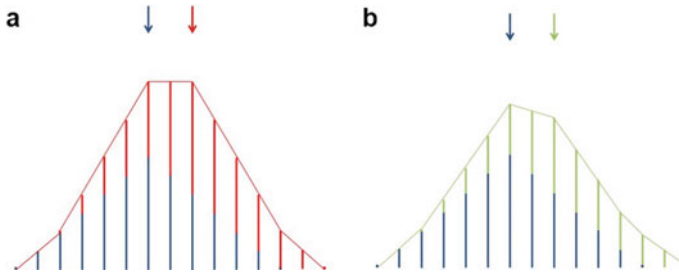


Fig. 27 Role of the impact angle on profile calculation from a starting profile in blue, **a** with no involvement of the impact angle for calculation of the subsequent profile (in red), **b** with involvement of the impact angle for calculation of the subsequent profile (in green)

will be conducted for a given spraying time, i.e. in iso-spraying time conditions in which the quantity of sprayed powder is the same.

4.2.1 Traverse Speed

Changing the traverse speed results in modifying the bead profile dimensions, i.e. bead width and bead height in a 2D cross-section. Since the width does depend on pressure, temperature and stand-off distance but not on the traverse speed, the height only has to be modified as a function of this latter parameter [70]. From experimental results showing that traverse speed has no effect on the (absolute) deposition efficiency for beads (Fig. 28), provided that the measurement errors are neglected, one can therefore state that the deposited material mass, i.e. bead height, is inversely proportional to the traverse speed. To set the definitions, one may note that, in contrast with the absolute deposition efficiency, the relative deposition efficiency compares to that obtained when spraying perpendicularly (spray angle of 90°), taken as 100%.

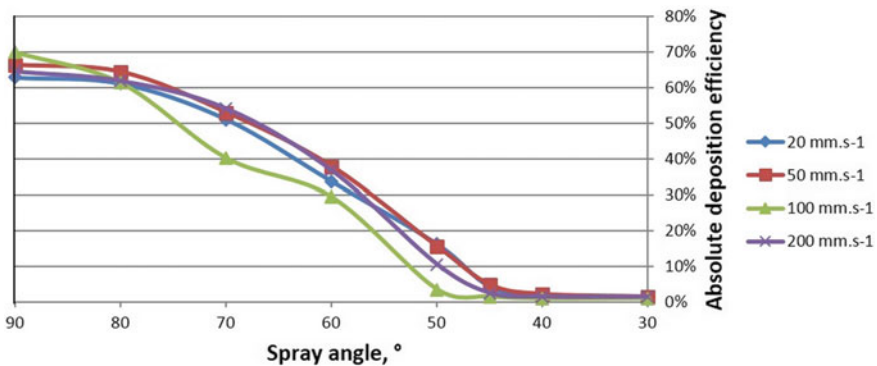


Fig. 28 Deposition efficiency versus spray angle curves for different traverse speeds

However, in iso-time conditions, the traverse speed shows a significant influence on deposit thickness, (Fig. 29). Moreover, the latter reaches a limit value after a certain traverse speed increase, e.g. approaching a thickness of 4.9 mm when above 50 mm s^{-1} typically. This can be explained easily by the fact that the thickness of

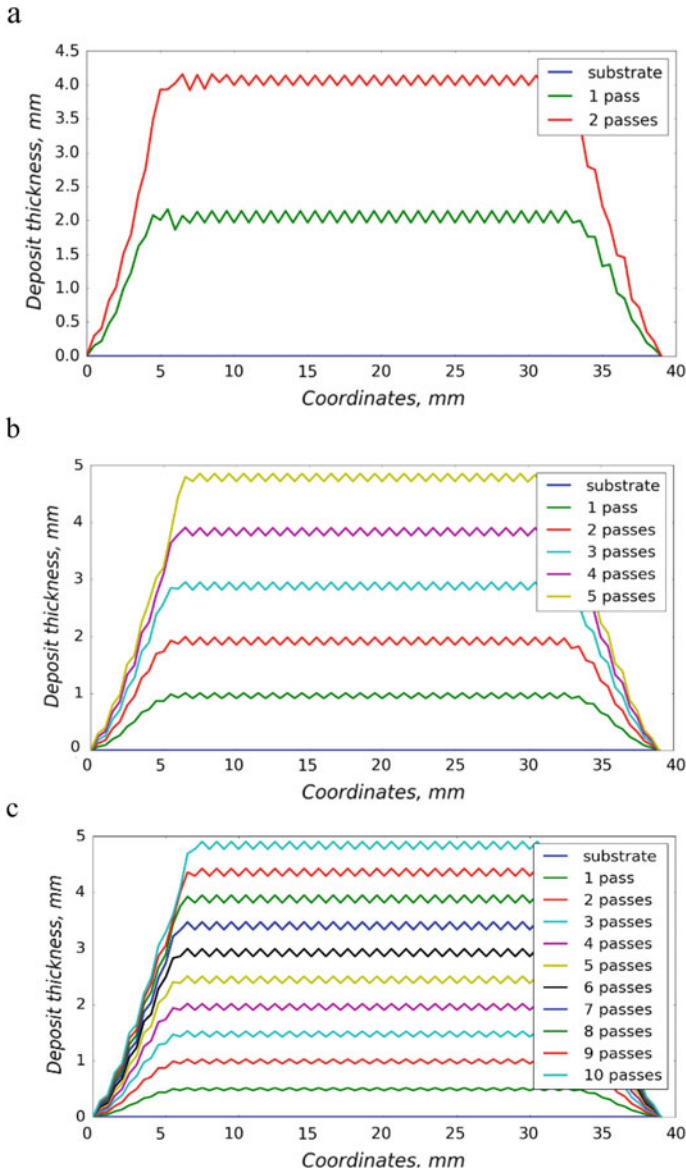


Fig. 29 Two-dimensional simulation of a deposit using a given step size of 1 mm, **a** 2 passes at a traverse speed of 20 mm s^{-1} , **b** 5 passes at 50 mm s^{-1} , **c** 10 passes at 100 mm s^{-1}

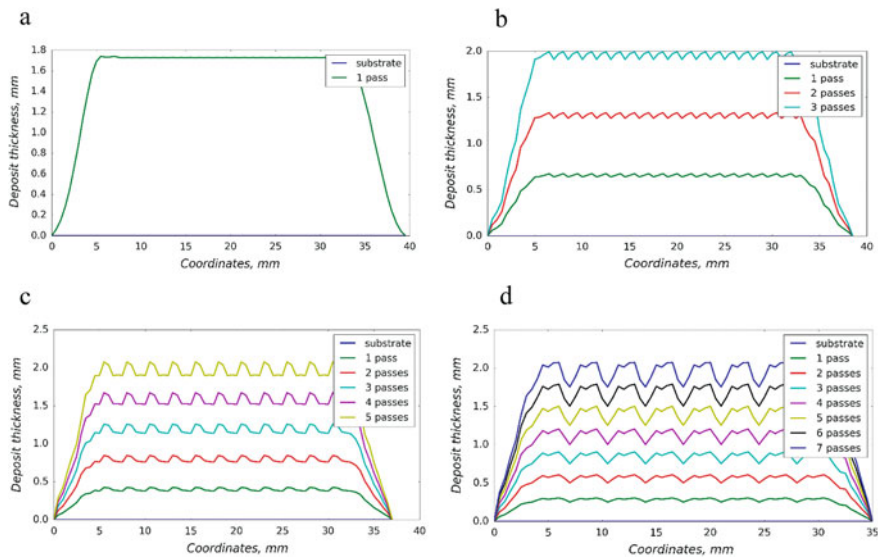


Fig. 30 Simulated profiles for a given traverse speed of 50 mm s^{-1} with, **a** a step size of 0.5 mm in 1 pass, **b** a step size of 1.5 mm in 3 passes, **c** a step size of 2.5 mm in 5 passes, **d** a step size of 3 mm in 6 passes

a given elementary bead pass is all the lower as the traverse speed is high, which corresponds to higher local spray angle for the successive beads (Fig. 29).

4.2.2 Nozzle Trajectory

Step Size

As already stated, any relevant comparison between deposits must be made for a given spraying time. Simulations are therefore developed for a given traverse speed with a number of passes to be selected as a function of the spatial shift. For example, doubling the step size leads to also double the number of passes.

The step size has little influence on deposit thickness compared to traverse speed unless it is restricted to very low values, due to the influence of the particle impact angle. The lower the step size, the steeper the bead profile is. In contrast, surface roughness does depend on the step size, both for the peak-to-valley ratio and for the profile itself (Fig. 30).

Unlike what can be seen for traverse speed, no clear trend emerges for the influence of the step size. Every case is particular. For a given traverse speed there is an optimal step size. For example, in the already-taken conditions for deposition of Al 2024 (see figures and previous sections), the optimal step size is 1.5 mm for a traverse speed of 50 mm s^{-1} though it is 1.0 mm for a speed of 20 mm s^{-1} .

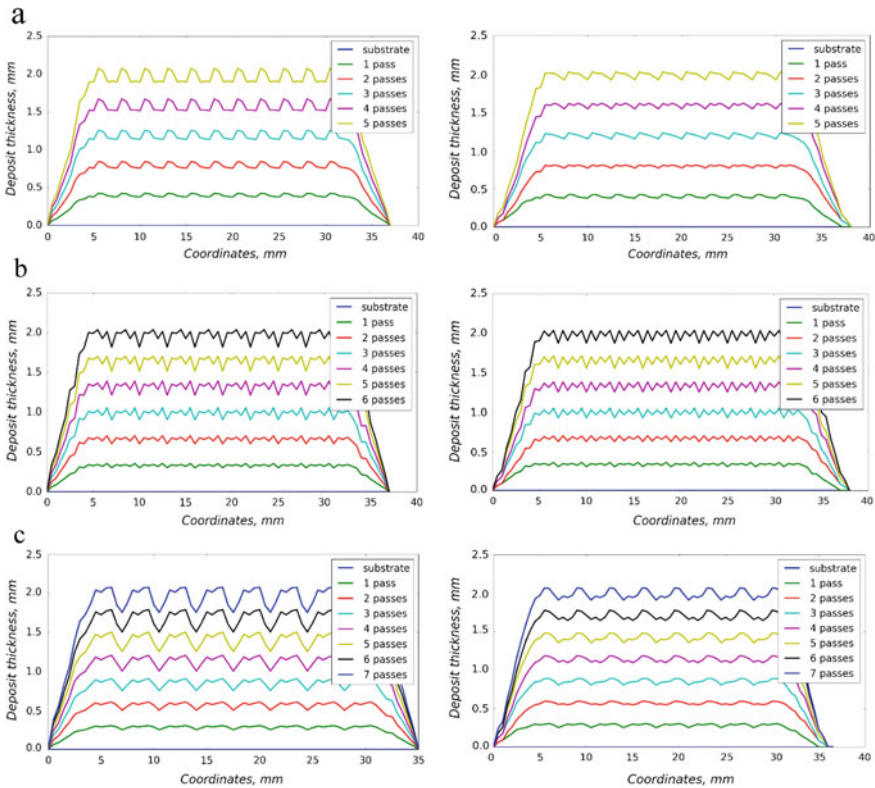


Fig. 31 Influence of a spatial shift of half the step size on the simulated bead profiles, at a traverse speed of 50 mm s^{-1} , for a step size of **a** 2.5 mm, **b** 3 mm, **c** 3.5 mm. Left diagrams, without shifting; Right diagrams, with shifting

Spatial Shift

The spatial shift between 2 successive passes, as defined in Fig. 24, can show an influence on surface roughness as done by the step size. These two parameters, as could be expected, are not independent. There is no systematic correlation. One may say that a spatial shift of half of the step size, typically, is beneficial for roughness, but the extent of improvement for this given spatial shift depends on the value of the step size. In the example of Fig. 31, for given thickness and traverse speed, the improvement is of a lesser extent for the intermediate value of the step size, i.e. 3 mm, compared to that obtained for 2.5 and 3.5 mm. Moreover, there is no improvement at all for a low value of step size such as 1 mm, insofar as the simulated curves with and without shifting are superimposable (no figure shown in this article). The improvement is not therefore systematic, the explanation of which is not yet elucidated, even though one may assume this might depend on simulation accuracy.

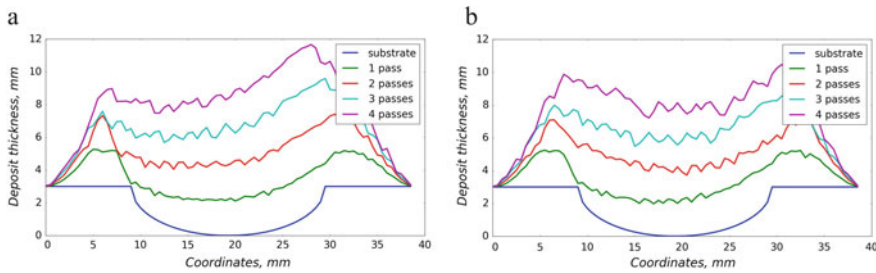


Fig. 32 Influence of the reversal of the nozzle direction of motion on the simulated bead profiles, for a traverse speed of 20 mm s^{-1} , a step size of 1 mm as a function of the number of passes (up to 4), **a** with no reversal, **b** with reversal

Reversal of the Nozzle Direction of Motion

The reversal of the nozzle direction of motion i.e. in alternate passing, has practically no influence when using a flat substrate. At best, a slight decrease in the depth of the valleys in the roughness profile can only be seen. In contrast, when using shaped substrates, such as those which were considered in the simulation development (see further Sect. 3.3), the effect of the reversal is much more exhibited, as can be expected intuitively, due to some symmetrizing in the deposition process (Fig. 32). For example, a hole (in a 2D representation) can be said to show 2 opposite slopes. When depositing, the first slope is accentuated as the second slope is reduced due to the previously-deposited material. The reversal in the motion can limit the problem.

4.3 Improvement of the Model

4.3.1 Multi-profile Simulation

To better reproduce the randomness of the surface of the sprayed deposit, a major improvement in the simulation can result from the use of a series of bead profiles, rather than one profile only as the first model input (see Sect. 3.1.1). The previous sections discussed results starting from 1 bead profile to better exhibit the influence of a given parameter or another.

When using a single typical bead profile, the final roughness of the deposit resulted from repeated processing of the same bead profile in the simulation. As can be expected, this leads to a sort of uniformity in the roughness distribution, which can be vanished when involving several beads (all the more efficient that they are numerous, 10–15 typically) (Fig. 33). These bead profiles come from cross-sections of a bead achieved in given spraying conditions.

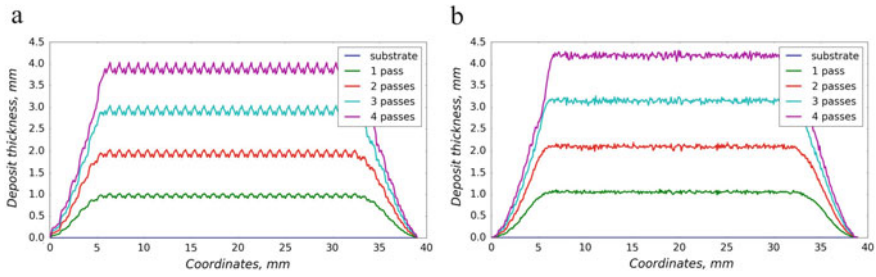


Fig. 33 Results from simulation using similar parameters but starting with, **a** 1 bead profile input, **b** several bead profiles

4.3.2 Extension to 3D Simulation

A 3D, or more exactly a pseudo-3D version of the build-up model was developed. The resulting surfaces are obtained from mere juxtaposition of the 2D profiles. However, the price to pay is that the impact angle in the direction parallel to that of the nozzle motion, i.e. the y axis, cannot be involved. This is not the case for the x axis, i.e. perpendicularly to the nozzle direction of motion. Consequently, there cannot be any slope in the y direction (Fig. 34).

In the y direction, changing the spraying direction also changes the spraying distance, which makes them hard to be discriminated. Moreover, depending on the nozzle direction of motion along this same axis, the effect of the spraying angle can be either promoted or reduced (Fig. 35).

This ascertained that the spraying angle was not involved deliberately in the development of this pseudo-3D simulation.

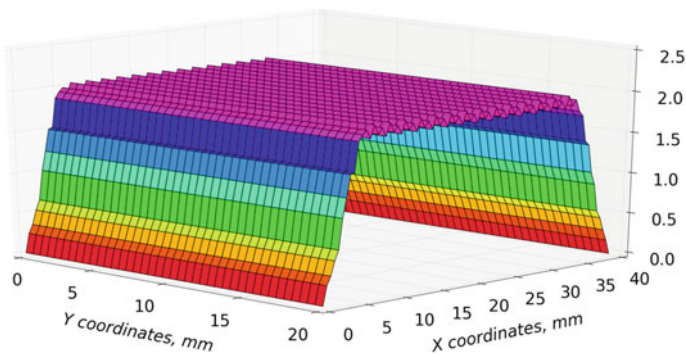
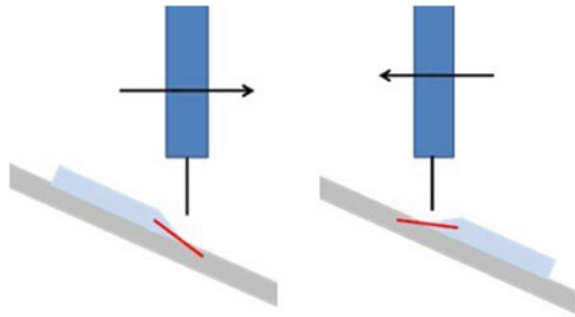


Fig. 34 Three-dimensional simulation of a 4-pass deposit for a traverse speed of 50 mm s^{-1} and a step size of 2 mm

Fig. 35 Schematic illustration of the influence of the spraying angle (shown by the red line) as a function of the nozzle direction of motion



4.4 Testing and Validation of the Model

Results are discussed using both 2D and 3D simulations. However, for testing and validating the fundamentals of the model/simulation, 2D is enough.

Validation mainly rests on testing the model when applied to shaped substrates. Three typical shapes, i.e. V, U and round shapes were tested.

As a general result, simulation can be claimed to be in keeping with experiments. For reasons of brevity, the subsequent discussion is given in the example of the V-shaped groove only. The consistency between experimental tests and simulation is ascertained by typical features such as dissymmetry of the deposit profile (Fig. 36).

Moreover, the lowest point at the bottom of the groove shows the same coordinates and the various slopes almost the same angles in both profiles. The sole but rather significant discrepancy between the two profiles relates to bumps which formed in the simulated left slope of the V (Fig. 36). The presence of these bumps is assumed to result from small errors which could cumulate after every nozzle pass.

Simulation is quite satisfactory, even for rather small-sized grooves, e.g. of 2 mm in width for 1 mm in depth. In this type of narrower grooves, most noticeable is a higher roughness in the valley (whatever the shape of the groove) for simulation compared to experimental results. Otherwise, simulated results compare well with experimental results which vary in the so-called “gray range” in Fig. 37.

Roughly speaking, the results are similar for the other shapes which were tested. For the semi-elliptical in particular, the experimental global profile and roughness are in keeping with simulation, provided that the groove width is significantly larger than the groove depth, e.g. 5 times higher typically. For the smallest slots, improvements can be expected from the use of smaller spraying spot and step sizes. More generally, the comparison between simulation and experimental results can be problematic for shapes with rather steep slopes and low impact angles. This pleads in favor of the development of miniaturization of spraying systems to be used in cold spray additive manufacturing specifically.

Based on 2D results, at this stage of development the build-up model used in simulation can already be deemed robust. Further three-dimensional approach ascertains this. In this pseudo-3D approach, the basis of which was described in Sect. 3.3,

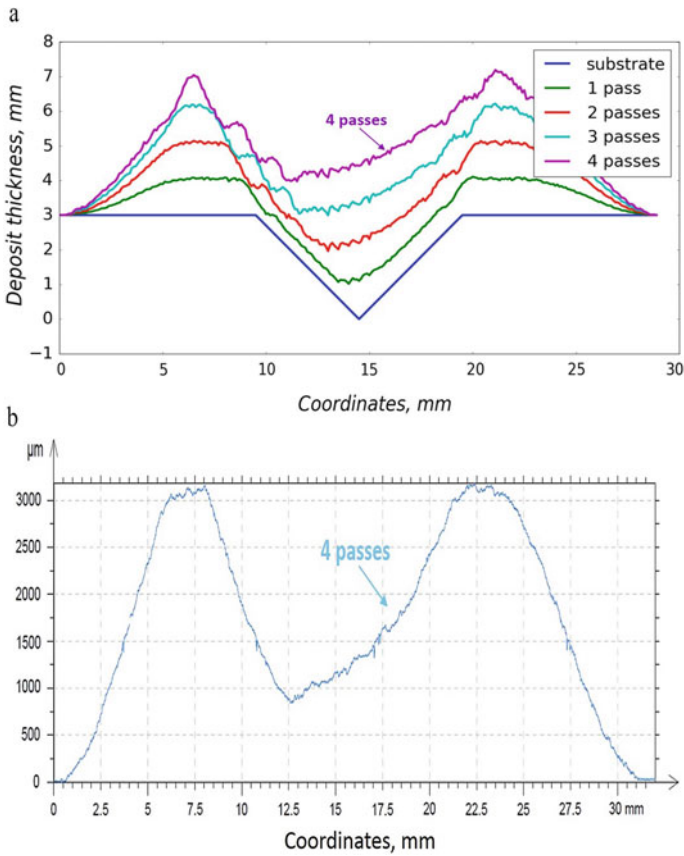


Fig. 36 Bead profile for a traverse speed of 50 mm s^{-1} , a step size of 1 mm, and 4 passes, onto a given V-grooved substrate, **a** simulated, **b** experimental

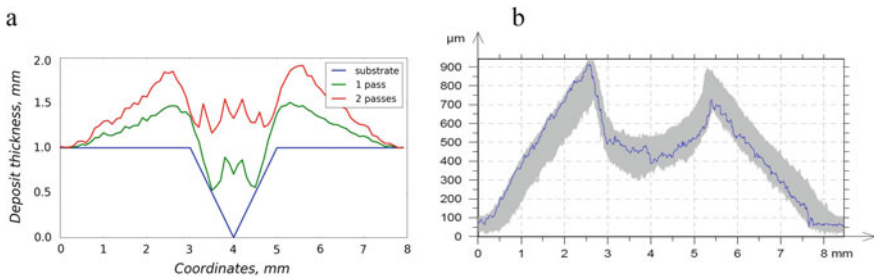


Fig. 37 Bead profiles for a traverse speed of 20 mm s^{-1} , a step size of 1 mm, and 2 passes, onto a given V-grooved substrate, **a** simulated, **b** experimental

numerous different 2D profiles were selected from a profile database for given bead conditions. Their number is taken high enough for relevant description of the deposit as a function of its size. The repeating number and order in the repeating process in the model are generated randomly. In these conditions, the model was also validated in 3D, based on results on the influence of the three following parameters, i.e. the step size, the traverse speed, and the shape of the substrate.

- Step size

For better visualization and comparison, results are given in the form of flat views for experimental roughness measurements and in the form of perspective views for simulated roughness.

For given spraying conditions, the ripple effect due to the influence of the step size in the robot trajectory is promoted when decreasing the step size from 2 to 1 mm (Fig. 38). This result ascertains that the model is valid, through the exhibiting of the influence of the step size and good consistency between simulated and experimental results regarding roughness ranges (width and peak-to-valley values).

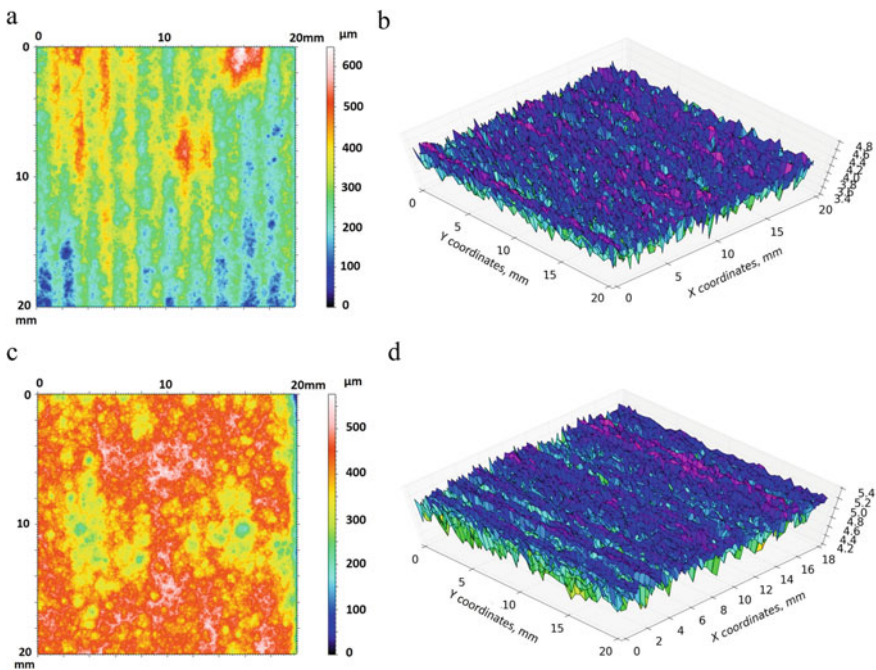


Fig. 38 Surface roughness of a $20 \times 20 \text{ mm}^2$ area for a traverse speed of 20 mm s^{-1} , **a** 2 passes with a step size of 1 mm, **b** corresponding simulation, **c** 4 passes with a step size of 2 mm, **d** corresponding simulation

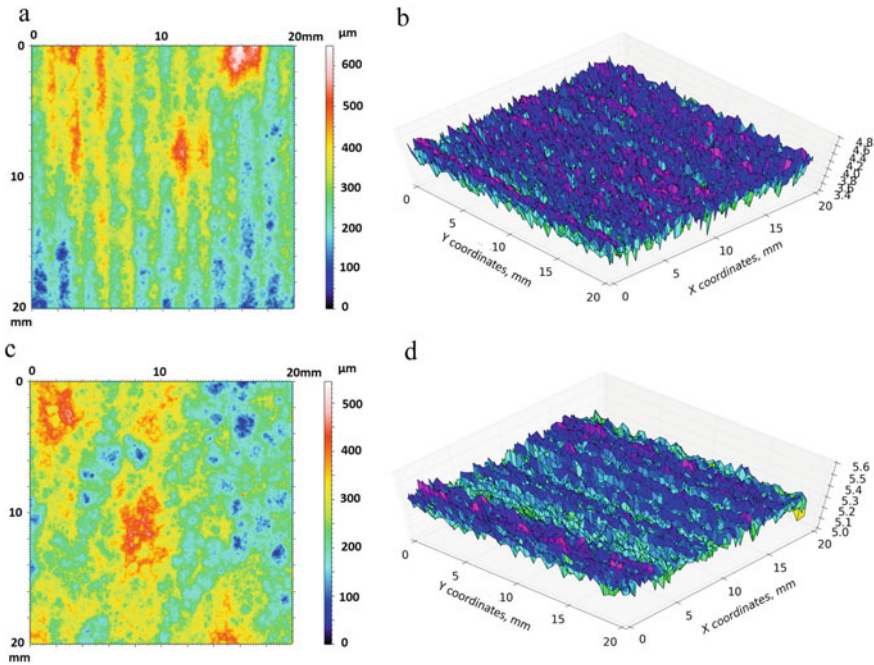


Fig. 39 Surface roughness of a $20 \times 20 \text{ mm}^2$ area for a step size of 1 mm, **a** 2 passes at a traverse speed of 20 mm s^{-1} , **b** corresponding simulation, **c** 5 passes at a traverse speed of 50 mm s^{-1} , **d** corresponding simulation

- Traverse speed

The conclusions on the influence of the traverse speed are similar to those for that of the step size, which can justify to merely copy/paste a good part of the previous section, that is, the ripple effect due to the influence of the traverse speed is promoted when decreasing the step size from 50 to 20 mm s^{-1} (Fig. 39). This result ascertains that the model is valid through the exhibiting of the influence of the traverse speed with good consistency between simulated and experimental results regarding roughness ranges (width and peak-to-valley values).

- Shape of the substrate

Three-dimensional profilometer data compare fairly well with simulation when applied to various shaped substrates, provided these are not too complex, i.e. within the already-mentioned limits. Otherwise, this should result in a case-by-case assessment (e.g. for a deep slot). Figure 40, even though different z scales do not make the comparison very easy, ascertains that the model is valid through the exhibiting of a good consistency between simulated and experimental results.

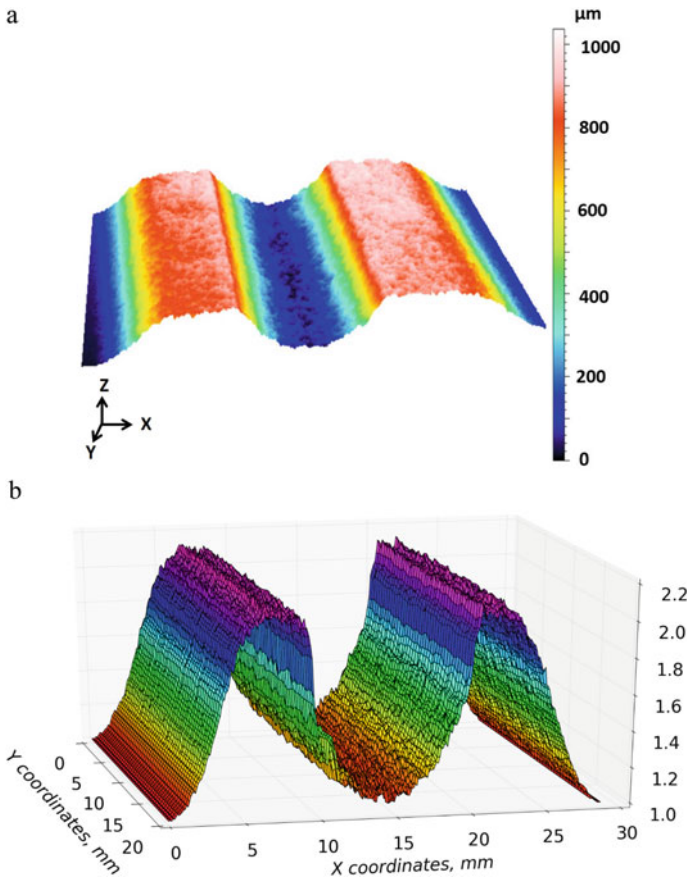


Fig. 40 Surface mapping of a deposit onto a U-shaped groove (elliptical, of 1 mm in depth and 10 mm in width), for 1 pass with a step size of 1 mm, **a** experimental, **b** simulated

4.5 Applications

Modeling at the scale of the deposit as shown in Sect. 3 of this chapter was shown to be suitable for predictive simulation of the shape and roughness of this same deposit. At the current stage of development, this type of simulation can be used for going faster, i.e. limiting the number of preliminary spraying experiments, in the establishing of relevant kinetic parameters and spraying conditions for a given application, i.e. given shape and thickness. A major asset of this type of simulation rests on the short computing time, i.e. a few minutes typically for mm-sized parts. For example, the simulated surface in Fig. 39b needs a computing time of no more than 6 s to be obtained. The development of this class of simulation can therefore be considered as a significant step on the road towards additive manufacturing.

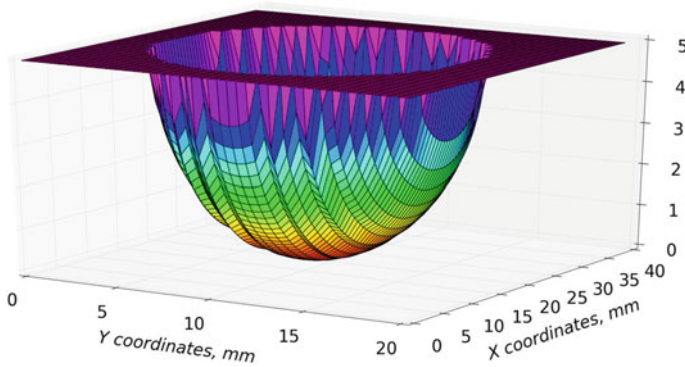


Fig. 41 Simulated surface of a hole prior to filling

A typical example of application is, for restoration/repair, that of filling a semi-ellipsoidal hole of 5 mm in depth, 30 mm in width along the x-axis and 15 mm in width along the y-axis (Fig. 41).

When fixing nominal spraying conditions including a traverse speed of 50 mm s^{-1} and a step size of 1 mm, simulation shows that 5 nozzle passes are not enough to fill the hole entirely (Fig. 42a, in which part of the deposit surface remains below the 5 mm z-plane) and that 6 passes are needed (Fig. 42b).

This build-up model needs no more than one minute to operate and leads to the simulation results shown in Fig. 42. A major asset rests on its capability in estimating the amount of powder to be used for a given application, since all the spraying parameters are known as inputs in the model. This results in an estimation of the spraying time and, consequently, of the amount of powder knowing the powder flow rate. In the previous example (Fig. 41), the filling of the considered hole needs about 16.1 g. Some discrepancy can however exist between estimation and actual powder consumption due to speed variation for the robot when changing direction. Moreover, some dead times such as that for the robot to reach the starting point for spraying are not involved in the estimation. Another consequence of any direction change for the robot is to reduce the reliability of the simulation, especially for deposit thickness prediction. This results from speed reduction for the robot, which leads to

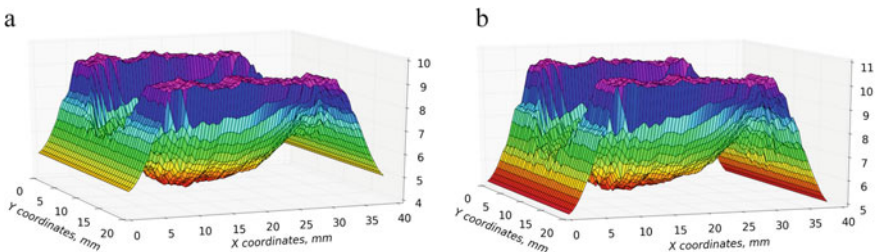


Fig. 42 Simulated surface of the hole shown in Fig. 41, **a** after 5 passes, **b** after 6 passes

some excessive build-up at the deposit edges. This effect is all the more pronounced as the robot moves fast.

5 Conclusion-Outlook

Cold spray additive manufacturing does need simulation/modeling of deposit build-up, whether it be for a mere coating or for direct manufacturing. An overview of modeling tools was given in this chapter, focusing on the most advanced approaches, which however still require development. This development is required due to extension of the range of materials which can be cold sprayed now (i.e. beyond conventional ductile powders), and to expectations from cold spray to achieve more and more complex shapes and higher properties. It is useless to say that all this must be done in the best possible cost effective conditions, i.e. with the best efficiency (powder consumption and productivity).

To be efficient for additive manufacturing using cold spray, these advanced tools for modeling of build-up issues, as shown in this chapter, have to be considered at two scales, i.e. that of the powder particle and that of the sprayed bead. Discussing build-up issues and related modeling/simulation tools resulted in the two main parts of the chapter. The philosophy behind the use of modeling in cold spray additive manufacturing is to claim that, depending on the targeted application and requirements, the user would have to use tools working either at the particle scale or at the bead scale. Moreover, as can be guessed, the best might be to combine both approaches, knowing the large variety of issues to be addressed in such a versatile process. This combination is all the more prominent because hybrid processes can also be envisaged for additive manufacturing, e.g. cold spray coupled with laser processing.

If there is just one thing to bear in mind in the development of these advanced models, this would be the crucial and often original contribution of the morphological approach to the sprayed materials (at both scales), which can involve the use of advanced tools from mathematical morphology.

In parallel with the development of modeling and simulation tools as shown in this chapter, one may infer from the content of this same chapter that action is required in two areas:

- *In the materials area:* Efforts should concentrate on the study of powder particle characteristics to be used as relevant input in build-up models. They relate to mechanical properties, morphology, physicochemistry, and metallurgy.
- *In the processing area:* The design of lower size cold spray components and facilities, not to say miniaturizing, must be developed to be in keeping with the scale over which the governing build-up phenomena occur and with the scale which are involved in the corresponding models.

Acknowledgements The authors would like to thank warmly Gilles Surdon and Kevin Roche from Dassault-Aviation/Mérignac, Erick Meillot from CEA/Le Ripault, and Pascal Lemeille from Mallard SA/Saint-Antoine-la-Forêt, all of them for technical assistance, fruitful discussions and financial support.

References

1. Ahmadian, S., Browning, A., & Jordan, E. H. (2015). Three-dimensional X-ray micro-computed tomography of cracks in a furnace cycled air plasma sprayed thermal barrier coating. *Scripta Materialia*, *97*, 3–16.
2. Amsellem, O., Borit, F., Jeulin, D., Guipont, V., Jeandin, M., Boller, E., et al. (2012). Three-dimensional simulation of porosity in plasma-sprayed alumina using microtomography and electrochemical impedance spectrometry for finite element modeling of properties. *Journal of Thermal Spray Technology*, *21*(2), 193–201.
3. Amsellem, O., Madi, K., Borit, F., Jeulin, D., Guipont, V., Jeandin, M., et al. (2008). Two-dimensional (2D) and three-dimensional (3D) analyses of plasma-sprayed alumina microstructures for finite-element simulation of Young's modulus. *Journal Materials Science*, *43*(12), 4091–4098.
4. Antoun, T., Seaman, L., Curran, D. R., Kanel, G. I., Razorenov, S. V., & Utkin, A. V. (2003). *Spall fracture*. New York, NY: Springer.
5. Armstrong, D. R., Borys, S. S., & Anderson, R. P. (1999). Method of making metals and other elements from the halid vapor of the metal. US Patent 5958106.
6. Armstrong, R., & Zerilli, F. (1994). Dislocation mechanics aspects of plastic instability and shear banding. *Mechanics of Materials*, *17*(2–3), 319–327.
7. Assadi, H., Irkhin, I., Gutzmann, H., Gärtner, F., Schulze, M., Villa Vidaller, M., et al. (2015). Determination of plastic constitutive properties of microparticles through single particle compression. *Advanced Powder Technology*, *26*(6), 1544–1554.
8. Bae, G., Xiong, Y., Kumar, S., Kang, K., & Lee, C. (2008). General aspects of interface bonding in kinetic sprayed coatings. *Acta Materialia*, *56*, 4858–4868.
9. Barradas, S., Guipont, V., Molins, M., Jeandin, M., Arrigoni, M., Boustie, M., et al. (2007). Laser shock flier impact simulation of particle-substrate interactions in cold spray. *Journal of Thermal Spray Technology*, *16*, 548.
10. Beauvais, S., & Decaux, O. (2007). Plasma sprayed biocompatible coatings on PEEK implants. In: *Proceedings of the International Thermal Spray Conference (ITSC '07)* (pp. 371–376), Beijing, China, May 14–16, 2007, ASM International.
11. Blochet, Q., Delloro, F., Borit, F., N'Guyen, F., Jeandin, M., Roche, K., & Surdon, G. (2014). Influence of spray angle on the cold spray of Al for the repair of aircraft components. In J. Jerzembeck et al. (Eds.), *Proceedings of the International Thermal Spray Conference and Exposition (ITSC'14)* (pp. 69–74), Barcelona, Spain, May 21–23, 2014. Düsseldorf: DVS Media GmbH. ISBN 978-3-87155-574-9.
12. Blochet, Q., Delloro, F., N'Guyen, F., Jeulin, D., Borit, F., & Jeandin, M. (2017). Effect of the cold-sprayed aluminum coating-substrate interface morphology on bond strength for aircraft repair application. *Journal of Thermal Spray Technology*, *26*(4), 671–686.
13. Bobzin, K., Ote, M., Knoch, M. A., Alkhasli, I., & Dokhanchi, S. R. (2019). Modelling of particle impact using modified momentum source method in thermal spraying. *IOP Conference Series: Materials Science and Engineering*, *480*, 012003.
14. Botef, I., & Villafuerte, J. (2015). Overview. In J. Villafuerte (Eds.), *Modern cold spray*. Cham: Springer.
15. Bunel, M., Borit, F., Delloro, F., Jeandin, M., Bacciocchini, A., Lemeille, P., et al. (2017). Experimental and numerical study of the influence of powder characteristics in the cold spraying

- of Al-based alloys for additive manufacturing using low-pressure, medium-pressure and high pressure cold spray facilities. In: *Proceedings of the International Thermal Spray Conference and Exposition (ITSC '17)* (pp. 714–718), Dusseldorf, Germany, 7–9 June 2017, ISBN: 978-1-5108-5822-0.
16. Cai, Z., Liang, H., Quan, S., Deng, S., Zeng, C., & Zhang, F. (2015). Computer-aided robot trajectory auto-generation strategy in thermal spraying. *Journal of Thermal Spray Technology*, 24(7), 1235–1245.
 17. Chen, Q., Alizadeh, A., Xie, W., Wang, X., Champagne, V., Gouldstone, A., et al. (2018). High-strain-rate material behavior and adiabatic material instability in impact of micron-scale Al-6061 particles. *Journal of Thermal Spray Technology*, 27, 641.
 18. Chen, S. R., & Gray, G. T. (1996). Constitutive behaviour of tantalum and tantalum-tungsten alloys. *Metallurgical and Materials Transactions A: Physical Metallurgy and Materials Science*, 27(10), 2994–3006.
 19. Cinca, N., Rebled, J. M., Estradé, S., Peiró, F., Fernández, J., & Guilemany, J. M. (2013). Influence of the particle morphology on the cold gas spray deposition behaviour of titanium on aluminum light alloys. *Journal of Alloys and Compounds*, 554, 89–96.
 20. Cochelin, E., Borit, F., Frot, G., Jeandin, M., Decker, L., Jeulin, D., et al. (1999). Oxidation and particle deposition modeling in plasma spraying of Ti-6Al-4 V/SiC fiber composites. *Journal of Thermal Spray Technology*, 8, 117.
 21. Cormier, Y., Dupuis, P., Jodoin, B., & Ghaei, A. (2015). Finite element analysis and failure mode characterization of pyramidal fin arrays produced by masked cold gas dynamic spray. *Journal of Thermal Spray Technology*, 24, 1549–1565.
 22. Delloro, F., Jeandin, M., Jeulin, D., Proudhon, H., Faessel, M., Bianchi, L., et al. (2017). A morphological approach to the modeling of the cold spray process. *Journal of Thermal Spray Technology*, 26, 1838–1850.
 23. Delloro, F., Jeandin, M., Faessel, M., Jeulin, D., Meillot, E., & Bianchi, L. (2014). A morphological approach to the modeling of the cold spray process. In J. Jerzembeck et al. (Eds.), *Proceedings of the International Thermal Spray Conference and Exposition (ITSC '14)* (pp. 221–225), Barcelona, Spain, 21–23 May, 2014. Düsseldorf, Germany: DVS Media GmbH. ISBN 978-3-87155-574-9.
 24. Descurninges, L. L., Mingault, L. T., Guipont, V., & Jeandin, M. (2011). Influence of powder particles oxidation on properties of cold sprayed tantalum. In J. Jerzembeck (Ed.), *Thermal Spray 2011: Proceedings of the International Thermal Spray Conference* (pp. 60–65), September 2011. DVS.
 25. Dosta, S., Bolelli, G., Candeli, A., Lusvarghi, L., Cano, I. G., & Guilemany, J. M. (2017). Plastic deformation phenomena during cold spray impact of WC-Co particles onto metal substrates. *Acta Materialia*, 124, 173–181.
 26. Everitt, B. S., Landau, S., Leese, M., & Stahl, D. (2011). *Cluster analysis* (5th ed.). Hoboken, NJ: Ed. Wiley.
 27. Fernandez, R., & Jodoin, B. (2018). Cold spray aluminum-alumina cermet coatings: Effect of alumina content. *Journal of Thermal Spray Technology*, 26, 1838–1850.
 28. Gama, B. A., Lopatnikov, S. L., & Gillespie, J. W. (2004). Hopkinson bar experimental technique: A critical review. *Applied Mechanics Reviews*, 57(4), 223–250.
 29. Ghafouri-Azar, R., Mostaghimi, J., Chandra, S., & Charmchi, M. (2003). A stochastic model to simulate the formation of a thermal spray coating. *Journal of Thermal Spray Technology*, 12(1), 53–69.
 30. Ghelici, R., Bagherifard, S., Guagliano, M., & Verani, M. (2011). Numerical simulation of cold spray coating. *Surface and Coatings Technology*, 205, 5294–5301.
 31. Gillibert, L., Peyrega, C., Jeulin, D., Guipont, V., & Jeandin, M. (2012). 3D multiscale segmentation and morphological analysis of X-ray microtomography from cold-sprayed coatings. *Journal of Microscopy*, 248(2), 187–199.
 32. Grujicic, M., Saylor, J. R., Beasley, D. E., DeRosset, W. S., & Helfritsch, D. (2003). Computational analysis of the interfacial bonding between feed-powder particles and the substrate in the cold-gas dynamic-spray process. *Applied Surface Science*, 219(3–4), 211–227.

33. Hassani-Gangaraj, M., Veysset, D., Nelson, K. A., & Schuh, C. A. (2018). In-situ observations of single micro-particle impact bonding. *Scripta Materialia*, 145, 9–13.
34. Hassani-Gangaraj, M., Veysset, D., Champagne, V. K., Nelson, K. A., & Schuh, C. A. (2018). Adiabatic shear instability is not necessary for adhesion in cold spray. *Acta Materialia*, 158(1), 430–439.
35. Ichikawa, Y., & Ogawa, K. (2015). Effect of substrate surface oxide film thickness on deposition behavior and deposition efficiency in the cold spray process. *Journal of Thermal Spray Technology*, 24(7), 1269–1276.
36. Ichikawa, Y., Tokoro, R., Tanno, M., & Ogawa, K. (2019). Elucidation of cold-spray deposition mechanism by auger electron spectroscopic evaluation of bonding interface oxide film. *Acta Materialia*, 164, 39–49.
37. Jeandin, M. (2011). A Socratic approach to surface modification: The example of thermal spray, Plenary talk. In E. Beyer, et al. (Eds.), *Proceedings of the 24th International Conference on Surface Modification Technologies (SMT 24)* (pp. 3–20), Dresden: Valardocs.
38. Jeandin, M. (2018). Cold spray under the banner of thermal spraying the whirlwind of additive manufacturing. *Surface Engineering*, 34(5), 341–343.
39. Jeandin, M., Koivuluoto, H., & Vezzu, S. (2015). Coating properties (Chap. 4). In J. Villafuerte (Ed.), *Modern cold spray materials, process, and applications*. Berlin: Springer.
40. Jeandin, M., Rolland, G., Descurninges, L. L., et al. (2014). Which powders for cold spray? *Surface Engineering*, 30, 291–298.
41. Johnson, G. R., & Cook, W. H. (1983). A constitutive model and data for metals subjected to large strains, high strain rates, and high temperatures. In *Proceedings of the 7th International Symposium on Ballistics* (pp. 541–547).
42. Johnson, G. R., & Holmquist, T. J. (1993). An improved computational constitutive model for brittle materials. In S. C. Schmidt, J. W. Shaner, G. A. Samara, & M. Ross (Eds.), *High Pressure Science and Technology-1993, AIP Conference Proceedings* (Vol. 309, pp. 981–984). New York, NY: AIP Press.
43. Jolliffe, I. T. (2001). *Principal Component Analysis* (2nd ed.). New York: Springer.
44. Khan, A. S., & Liang, R. (1999). Behaviors of three BCC metal over a wide range of strain rates and temperatures: experiments and modeling. *International Journal of Plasticity*, 15(10), 1089–1109.
45. Khan, A. S., & Liang, R. (2000). Behaviors of three BCC metals during non-proportional multi-axial loadings: Experiments and modeling. *International Journal of Plasticity*, 16(12), 1443–1458.
46. Knotek, O., & Elsing, R. (1987). Monte Carlo simulation of the lamellar structure of thermally sprayed coatings. *Surface & Coatings Technology*, 32(1–4), 261–271.
47. Li, W., Liao, H., Li, C., Bang, H., & Coddet, C. (2007). Numerical simulation of deformation behavior of Al particles impacting on Al substrate and effect of surface oxide films on interfacial bonding in cold spraying. *Applied Surface Science*, 253(11), 5084–5091.
48. Li, W. Y., & Gao, W. (2009). Some aspects on 3D numerical modeling of high velocity impact of particles in cold spraying by explicit finite element analysis. *Applied Surface Science*, 255, 7878–7892.
49. Li, W. Y., Yin, S., & Wang, X. F. (2010). Numerical investigations of the effect of oblique impact on particle deformation in cold spraying by the SPH method. *Surface Science*, 256(12), 3725–3734.
50. Lin, E., Chen, Q., Ozdemir, O. C., & Müftü, S. (2018). Effects of interface bonding on the residual stresses in cold sprayed Al-6061: A numerical simulation. In F. Azarmi, et al. (Eds.), *Proceedings of the International Thermal Spray Conference (ITSC 2018)* (pp. 278–295), May 7–10, 2018, Orlando, Florida, USA.
51. Liu, H., Lavernia, E. J., & Rangel, R. H. (1993). Numerical simulation of impingement of molten Ti, Ni, and W droplets on a flat substrate. *Journal of Thermal Spray Technology*, 2, 369–378.
52. MacDonald, D., Fernández, R., Delloro, F., & Jodoin, B. (2017). Cold spraying of armstrong process titanium powder for additive manufacturing. *Journal of Thermal Spray Technology*, 26, 598.

53. Manap, A., Okabe, T., & Ogawa, K. (2011). Relationship between particle size and deformation in the cold spray process. *Applied Surface Science*, *10*, 1145–1150.
54. Manap, A., Ogawa, K., & Okabe, T. (2012). Numerical analysis of interfacial bonding of Al-Si particle and mild steel substrate by cold spray technique using the SPH method. *Journal of Solid Mechanics and Materials Engineering*, *6*, 241–250.
55. Martin, M., & Vo, P. (2019). Advanced robot path planning for cold spray additive manufacturing. In *Proceedings of the CASI AERO Conference 2019* (p. 174). Available via https://www.openconf.org/aero2019/modules/request.php?module=oc_proceedings&action=summary.php&id=174&a=Accept. Accessed June 2, 2019.
56. Moridi, A., Gangaraj, S. M. H., Vezzu, S., & Guagliano, M. (2014). Number of passes and thickness effect on mechanical characteristics of cold spray coating. *Procedia Engineering*, *74*, 449–459.
57. Moridi, A., Hassani-Gangaraj, S. M., Guagliano, M., et al. (2014). Cold spray coating: review of material systems and future perspectives. *Surface Engineering*, *30*, 369–395.
58. Mukherjee, D., & Zohdi, T. I. (2015). A discrete element based simulation framework to investigate particulate spray deposition processes. *Journal of Computational Physics*, *290*, 298–317.
59. Nastic, A., Vijay, M., Tieu, A., Rahmati, S., & Jodoin, B. (2017). Experimental and numerical study of the influence of substrate surface preparation on adhesion mechanisms of aluminum cold spray coatings on 300 M steel substrates. *Journal of Thermal Spray Technology*, *26*, 1461–1483.
60. Parra Denis, E., Barat, C., Jeulin, D., & Ducottet, C. (2008). 3D complex shape characterization by statistical analysis: application to aluminium alloys. *Materials Characterization*, *59*, 338–343.
61. Pasandideh-Fard, M., & Mostaghimi, J. (1995). On the spreading and solidification of molten particles in a plasma spray process effect of thermal contact resistance. *Plasma Chemistry and Plasma Processing*, *16*(S1), S83–S98.
62. Pattison, J., Celotto, S., Morgan, R., Bray, M., & O'Neill, W. (2007). Cold gas dynamic manufacturing: A non-thermal approach to freeform fabrication. *International Journal of Machine Tools and Manufacture*, *47*(3–4), 627–634.
63. Preston, D. L., Tonks, D. L., & Wallace, D. C. (2003). Model of plastic deformation for extreme loading conditions. *Journal of Applied Physics*, *93*(1), 211–220.
64. Rahmati, S., & Ghaei, A. (2014). The use of particle/substrate material models in simulation of cold-gas dynamic-spray process. *Journal of Thermal Spray Technology*, *23*(3), 530–540.
65. Raelison, R. N., Verdy, C., & Liao, H. (2017). Cold gas dynamic spray additive manufacturing today: Deposit possibilities, technological solutions and viable applications. *Materials and Design*, *133*, 266–287.
66. Rolland, G. (2011). Laser-induced damage in cold-sprayed composite coatings. *Surface and Coatings Technology*, *205*, 4915–4927.
67. Sabard, A., de Villiers Lovelock, H. L., & Hussain, T. (2018). Microstructural evolution in solution heat treatment of gas-atomized Al alloy (7075) powder for cold spray. *Journal of Thermal Spray Technology*, *27*(1–2), 145–158.
68. Schmidt, T., Gärtner, F., Assadi, H., & Kreye, H. (2006). Development of a generalized parameter window for cold spray deposition. *Acta Materialia*, *54*(3), 729–742.
69. Sunil, P., & Gobinda, S. C. (2017). Development of sustainable cold spray coatings and 3D additive manufacturing components for repair/manufacturing applications: A critical review. *Coatings*, *7*(8), 1–27.
70. Trifa, F. I., Montavon, G., & Coddet, C. (2007). Model-based expert system for design and simulation of APS coatings. *Journal of Thermal Spray Technology*, *16*(1), 128–139.
71. Trinchi, A., et al. (2011). Copper surface coatings formed by the cold spray process: Simulations based on empirical and phenomenological data. *Journal of Thermal Spray Technology*, *20*(5), 986–991.
72. Vardelle, M., Vardelle, A., Leger, A. C., Fauchais, P., & Gobin, D. (1995). Influence of particle parameters at impact on splat formation and solidification in plasma spraying processes. *Journal of Thermal Spray Technology*, *4*(1), 50–58.

73. Vardelle, A., Moreau, C., Akedo, J., Ashrafizadeh, H., Berndt, C. C., Berghaus, J. O., et al. (2016). The 2016 thermal spray roadmap. *Journal of Thermal Spray Technology*, 25(8):1376–1440.
74. Vo, P., & Martin, M. (2017a). Layer-by-layer buildup strategy for cold spray additive manufacturing. In J. Jerzembeck, et al. (Eds.), *Proceedings of the 2017 International Thermal Spray Conference* (pp. 714–718). Düsseldorf: DVS Media GmbH.
75. Vo, P., & Martin, M. (2017b). Layer-by-layer buildup strategy for cold spray additive manufacturing. Pdf presentation available via https://www.coldsprayteam.com/Vo_Martin_CSAT2017%20Vo%20and%20Martin%20vfinal.pdf. Accessed June 2, 2019.
76. Weiller, S., Debray, A., Gaslin, F., Sennour, M., Delloro, F., Jeandin, M., & Garion, C. (2019). Cold spray as an innovative process to develop leak tight aluminum coatings for ultrahigh vacuum applications in a large particle high-energy collider. In F. Azarmi, et al. (Eds.), *Proceedings of the International Thermal Spray Conference (ITSC 2019)* (pp. 831–837), May 26–29, 2019, Yokohama, Japan.
77. Wu, H., Xie, X., Deng, S., & Liao, H. (2019). A new approach to simulate coating thickness in cold spray. In F. Azarmi, et al. (Eds.), *Proceedings of the International Thermal Spray Conference* (pp. 165–171), May 26–29, 2019, Yokohama, Japan.
78. Xie, J., Nélias, D., Walter-Le Berre, H., Ogawa, K., & Ichikawa, Y. (2015). Simulation of the cold spray particle deposition process. *Journal of Tribology*, 137(4).
79. Zerilli, F. J., & Armstrong, R. W. (1987). Dislocation-mechanics-based constitutive relations for material dynamics calculations. *Journal of Applied Physics*, 61(5), 1816–1825.